2014

Numerical Simulation of Nanoparticle Transportation and Deposition in Pulmonary Vasculature

Junda Zheng
Lehigh University

Numerical Simulation of Nanoparticle Transportation and Deposition in Pulmonary Vasculature

by Junda Zheng

A Thesis

Presented to the Graduate and Research Committee

of Lehigh University

in Candidacy for the Degree of

Master of Science

in

Department of Mechanical Engineering and Mechanics

Lehigh University

May-2014

Thesis is accepted and approved in partial fulfillment of the requirements for the Master of Science in Department of Mechanical Engineering and Mechanics.

Numerical Simulation of Nanoparticle Transportation and Deposition in Pulmonary Vasculature

Junda Zheng

_____

Date: May 2014

_____

Thesis Advisor: (Yaling Liu)

_____

Chairperson of Department: (Gary Harlow)

ACKNOWLEDGMENTS

Firstly, I would like to thank my adviser Dr. Yaling Liu for the continuous support of my M.S. study and research. His mentoring in research, his thorough knowledge, patience and motivation helped me a lot in writing the thesis. Without his guidance and support, the thesis would not have been possible.

Secondly, I want to express my appreciation to all my lab mates including but not limited to Jifu Tan, Shunqiang Wang, Yihua Zhou, Salman Sohrabi, Doruk Yunus and Christopher Uhl. It is joyful to work with you. And this acknowledgement will remain incomplete without thanking the reliable and efficient support of administrative staff of Mechanical Engineering and Mechanics Department.

Finally, I would like to thank my parents for their supports on my studying over the last 25 years. I love you all.

Table of Contents

List of Figures

List of Tables

Abstract

Nanoparticle holds significant promise as the next generation of drug carrier that can realize targeted therapy with minimal toxicity. To improve the delivery efficiency of nanoparticles, it is important to study their transport and deposition in blood flow. Many factors, like particle size, vessel geometry and blood flow rate, have significant influence on the particle transport, thus on the deposition fraction and distribution.

In this thesis, computational fluid dynamics (CFD) simulations of blood flow and drug particle deposition were conducted in four models representing the human lung vasculature: artificial artery geometry, artificial vein geometry, original geometry and over-smoothed original geometry. Flow conditions used included both steady-state inlet flow and pulsatile inlet flow. Parabolic flow pattern and lumped mathematic model were used for inlet and outlet boundary conditions respectively. Blood flow was treated as laminar and Newtonian. Particle trajectories were calculated in each of these models by solving the integrated force balance on the particle, and adding a stochastic Brownian term at each step. A receptor-ligand model was integrated to simulate the particle binding probability. The results indicate the following: (i) Pulsatile flow can accelerate the particle binding activity and improve the particle deposition fraction on bifurcation areas; (ii) Unlike drug delivery in lung respiratory system, particle diffusion is very weak in blood flow, no clear relationship between the particle size and deposition area was found in our four-generation lung vascular model; and (iii) Surface imperfections have the dominant effect on particle deposition fraction over a wide range of particle sizes. Ideal artificial geometry is not sufficient to predict drug deposition, and an accurate image based geometry is required.

Chapter 1

Introduction

This thesis work focus on the development of a computational model for nanoparticle transport and deposition in pulmonary vasculature. In this chapter, pulmonary drug delivery, the application of nanoparticle on medicine, various nanoparticles properties, motivations to do the study and proposed work are addressed.

1.1 Pulmonary Drug Delivery

Due to the advantages that the lung has a large absorptive surface area but extremely thin absorptive membrane and good blood supply, pulmonary drug delivery has gained growing attention as a non-invasive administration for systemic delivery of drug. Aerosol inhalation technique is commonly utilized in drug administration. Jet or ultrasonic nebulizers, meterd-dose inhaler (MDI) and dry-power-inhaler (DPI) are three commonly used clinical aerosols. Aerosol is deposited in the airways by diffusion, gravitational sedimentation and inertial impaction. The bioavailability and delivery efficiency can be modified by many factors, like aerosol particle size, shape, and surface chemical properties. Now, many inhalers products are available in Europe and USA, like Airomir, Asmol, Qvar, Ventolin and etc [1]. To spread drug throughout the airspace of lungs more evenly, a novel concept to deliver drugs by using perfluorocarbon liquid is proposed recently. By this way, up to 100 times more active substance can be delivered to the diseased lungs. Despite the recognized advantages of pulmonary drug delivery system has been exploited, it still be limited mostly to treatment of lung-associated diseases, like asthma, cystic fibrosis and respiratory infection for a long time. Until recent few decades, broader utilities of either localized or systemic delivery of drug from lung vasculature receive as much attention as it deserved [2]. Until 1990, the first descriptions of inhaled insulin for treatment of diabetes patients was recorded. The

advantages over injections were not only in term of patient compliance but also in terms of increased bioavailability.

1.2 Application of Nanoparticle in medicine

The biological and medical communities have developed various applications based on the unique properties of nanomaterials, like contrast agents for cell imaging and therapeutics for cancer treatment. These unique properties and potential applications offered by nanoparticles attract the attentions of scientists, engineers and medical researchers. For example, nanoparticles can imbibe drug into their core or coat drug into their surface to fight against cardiovascular disease and various cancers. Their half time in circulation and deposition distribution can be modulated by their size and shape which can be easily achieved by advanced micro-fabrication technology. The drug release process can even be controlled by other external properties like PH, temperature or magnetic field. Over the past decade, we have witnessed so many researches and developments of nanoparticulate system for diagnostic imaging and targeted therapeutic applications [3-9]. Various nanoplatforms, including liposomes [10,11], polymeric micelles [12-14], quantum dots [15,16], Au/Si/polymer shells [17-19], and detrimers [20-22] have been established to develop smart drug carriers. These technologies have provided the possibility of delivering drugs to specific cells, which is also called targeted drug delivery. The goal of targeted drug delivery is to localize, prolong, target and have a controllable drug interaction with the diseased tissue. By this way, we can reduce the frequency of the dosages taken by patients, drug side-effects and the fluctuation in circulating drug levels. In April 2006, 130 nanotech-based drugs and delivery systems were being developed worldwide [23]. Nanomedicine sales reached $6.8 billion in 2004, with over 200 companies and 38 products worldwide. A minimum of $3.8 billion is being invested in nanotechnology R&D every year [24]. As the nanomedicine industry continues to grow, it will surly have a significant impact on the economy.

1.3 Engineered Nanoparticle Properties

Properties such as size, shape, surface chemistry play an important role in nanoparticle transport and deposition. Size, as a key characteristic of nanoparticles has been extensively studied in literature. For example, it is well known that spherical particles bigger than 200nm can be easily filtered by the liver. On the other side, particles smaller than 10nm can be quickly cleared by the kidney or through extravasation. Thus, particles with diameters of 10-200nm are the ideal drug carriers in vascular circulation system [25]. Similar to size, shape is also a fundamental property of nanoparticles. For example, it is reported that non-spherical shape particles have remarkably higher adhesion probability, comparing to spherical for a given particle volume [26]. Fig. 1.1& 1.2 shows some products of nanoparticles with different sizes and shapes. What's more, according to the study of Geng *et al*. [27], non-spherical particle has higher chances of survival during the circulation in vascular system compare to its counterpart spherical ones. Besides size and shape, surface functionalization of nanoparticle also determines the adhesion capability of nanoparticles. For nanorods, it is reported that compared to uniform coating, Janus coating at the two ends of nanorods leads to better adhesion [28,29]. By the immobilization of polyethylene glycol (PEG), protein adsorption and phagocytosis of particles *in vivo* would decrease [30].

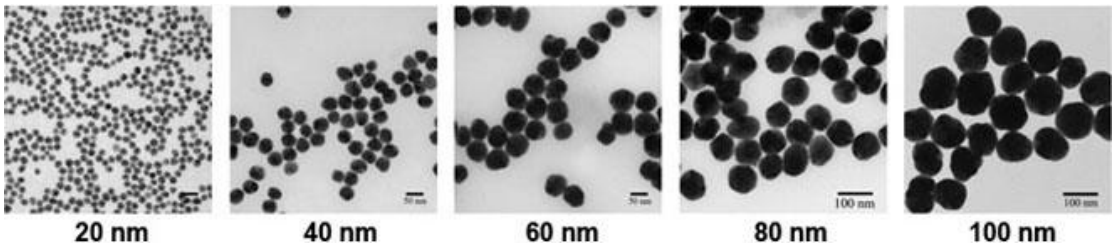

Figure 1.1 BioPure Silver and Gold NPs from
http://nanocomposix.com/kb/nanotoxicology/particle-selection

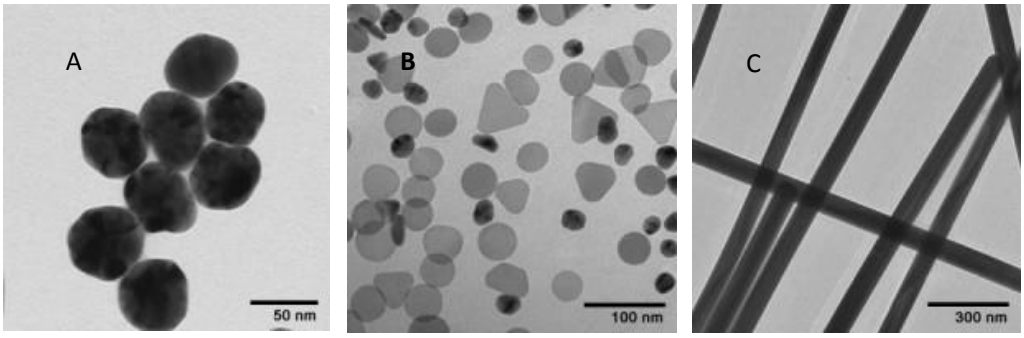

Figure 1.2 A: BioPure silver nanospheres; B: nanoComposix silver; C: nanoComposix silver nanowires nanoplates from http://nanocomposix.com/kb/nanotoxicology/particle-selection

1.4 Motivations to Model Nanoparticle Transportation and Deposition

Although nanoparticles offer more advantages than other conventional drug carriers, their transport and deposition in human vasculature have not been fully understood. One reason is that nanoparticles are too small to be visualized and tracked by experiments *in vivo*. Another is that the biological environment *in vivo* is very complex for nanoparticles. To achieve better delivery efficacy, many factors, including the diseased area type, size, location and the patient's physical parameters (e.g. vascular diameter, blood flow rate and etc.), should be considered. It is very challenging to study only one or two factors' influence and keep other parameters same by experiment *in vivo*. However, validated computational fluid-particle dynamics (CFPD) simulations provides us a non-invasive, accurate and cost-effective means to obtain such information.

Size, as a key characteristic of nanoparticles, directly influences the mechanism of deposition. For large particle, like micron particles, the main deposition mechanism is inertia effect. For smaller particle, like sub-micron particles, Brownian motion becomes stronger and dominantly affects the result. Besides that, other factors, including particle shape, fluid viscosity, fluid velocity, heart rate and vascular geometry, should be considered as well. Many researches have been conducted on how particle size, shape and velocity influence its transport and delivery. For example, J. Tan *et al*. [31], B. Asgharian *et al*. [32], Toby Lai [33] and Barbara M. Johnston *et al*. [34]. Either simple

bifurcate branch or symmetric simulated ideal model is used in their studies to characterize the effects of nanoparticles properties. For example, it was reported that nanoparticles with smaller size bind fast than bigger ones, because diffusion coefficient is inversely proportional to the particle size in Y. Liu [26]. In that paper, only 10nm and 100nm particles have been studied in capillary vessel with diameter of 10μm and 20μm. The author did not give out a method to link the micro-scale particulate model with multi-scale model of organ level. The latter is more beneficial to nanoparticle distribution prediction and drug dosage administration.

It is not trivial to reconstruct a large scale vasculature network and input into computational model. The geometry of the model does have significant influence on the fluid velocity field, thus on the particle transportation and deposition. Some phenomena are even contradictory in realistic model and artificial model, reported by Natalya Nowak *et al*. [35]. In the paper, they simulate the micro-particles delivery and deposition in human lung airway and compare the result between artificial model and realistic human trachea model. The result shows more particles stick at straight vessel in realistic trachea model, which is opposite to that in an artificial model. In an artificial model, because of the relatively smoother and more symmetric geometry, almost no particle sticks at straight vessel wall. The influence of complex geometry is also reported by B. Asgharian [32]. When particle size is small, the loss mechanisms are due to sedimentation and diffusion combined. More particles deposit in lower airways, and this pattern is the same in all geometries. But, when particle size is large, the main loss mechanism is impaction, which is strongly dependent on geometry. More particles deposit in upper airways in the stochastic model, which is different in other two symmetric models where particles still deposit more in lower parts. So a realistic 3-D vascular model is necessary, if we want to do a more realistic simulation for drug delivery.

Many angiographic image processing methods are reported in literatures, and two of them can be distinguished [36]. One is a global approach, aimed at automatically recognizing vessel skeletons on angiograms and at reconstructing an entire stationary or moving vascular tree. No detailed information on the local shape of vessels is needed.

Another one is a local approach, aimed at accessing the accurate 3-D geometry of a complex stenosed single or bifurcation vascular segment observed by radiologists, in order to extract quantitative parameters and qualitative information on vessel morphology. However, due to the limitation of CT or MRI scan technology, numerical reconstruction work is challenging. Although current image technology can get a vascular image up to 9 or 10 generation, reconstruction work for that is very difficult. The geometry beyond generation 5 is not likely to be accurate, according to Natalya Nowak [35], due to the limitation of MRI or CT resolution and the movement of patient during the scan procedure. Pathological irregular single or double cross-sectional shape may occur in the area of sudden lesion disruption or lumen occlusion. Also, because of the low MRI resolution, the image reconstructed by medical modeling software is always coarse and disconnected in small vessel part. To solve these problems, some methods have been proposed [36, 37]. Deformable model is commonly used. The algorithm consists of two steps: first, an initial model is built, based on the elliptic approximation that is valid for healthy single vessels and concentric stenosis, and then a deformation of the ellipse controlled by an optimization algorithm is applied in order to fit any pathological or branching cross-section [36].

Computational fluid dynamic (CFD) simulation provides an attractive way to study the particle delivery on complex geometry model. Some examples are presented in Z. Zhang *et al*. [38], Ming-Jyh Chern *et al*. [39], and Jeffry D. Schroeter *et al*. [40]. High computational cost for the numerical simulation of large scale model is another problem. Thus, in most of current studies, either symmetric artificial geometry or small subunit of complex realistic geometry is used.

1.5 Proposed Work

In this paper, two artificial model and a realistic subunit of pulmonary vascular model reconstructed from the left lung MRI image are considered. Blood flow is treated as Newtonian and laminar fluid flow. Particle is tracked as discrete phase particle by integrating the force balance on the particle. A fully developed physiological velocity

profile is defined as the vascular inlet boundary condition. To overcome the incompleteness of vascular system, a proper pressure condition for the outlets is developed where a lumped mathematical model is derived to calculate the overall resistance at each outlet. A shear rate and particle size dependent ligand-receptor model [41] is used to define the particles binding probability.

The objective of this paper are twofold: (1) reconstruct a realistic 3D pulmonary vascular model from MRI image, apply appropriate and boundary conditions, and develop a multi-scale approach for nanoparticle delivery in the 3D model; (2) characterize the effects of particle size, vascular geometry , and blood velocity on the drug particle transportation and deposition. In the following part of this paper, we will first introduce a pulmonary vascular geometry reconstruction method, then develop an approach to do CFD simulations for particle transport and deposition, and finally characterize the effects of some key factors which affect drug delivery efficiency based on the simulation result.

Chapter 2

Numerical Modeling

In this chapter, reconstruction of pulmonary geometry, governing equation for blood flow, particles transport theories and the proper boundary condition will be introduced.

2.1 Reconstruction of pulmonary geometry

To study the influence of vascular geometry on particles deposition, four different lung models are built in this research. The first one is an artificial artery model, the second one is an artificial vein model, the third one is a realistic lung model with the original rough surface obtained from MRI image, and the last one is the same realistic lung model with an over-smoothed surface. Different softwares such as Vascular Modeling Toolkit (VMTK), Geomagic Studio and Inventor are used to reconstruct model structures. Moreover, ICEM-CFD is utilized for mesh generation.

2.1.1 Artificial Geometry

To construct the three-dimensional artificial lung model, two assumptions are made: (1) the branching angel at each bifurcation is 60 degree, and (2) the angel of rotation of the plane of the bifurcation originating in each daughter branch is 90 degree [35]. Here, a four generations subunit artery model and a five generations subunit vein model are built in Invertor as shown in Fig. 2.1A & B. The length and diameter of each generation is shown in Table 2.1. However, because of the different diameters of parent and daughter vessels, it would lead to discontinuities at the bifurcations. So another assumption is made here: different generation branch are connected by a frustum. The large diameter of the frustum is set to be equal to the diameter of the parent branch and

the small diameter of the frustum equal to the diameter of the daughter branch. The length of the frustum is set to make the upper surfaces (circles) of the two daughter branches tangential, as shown in Fig. 2.2

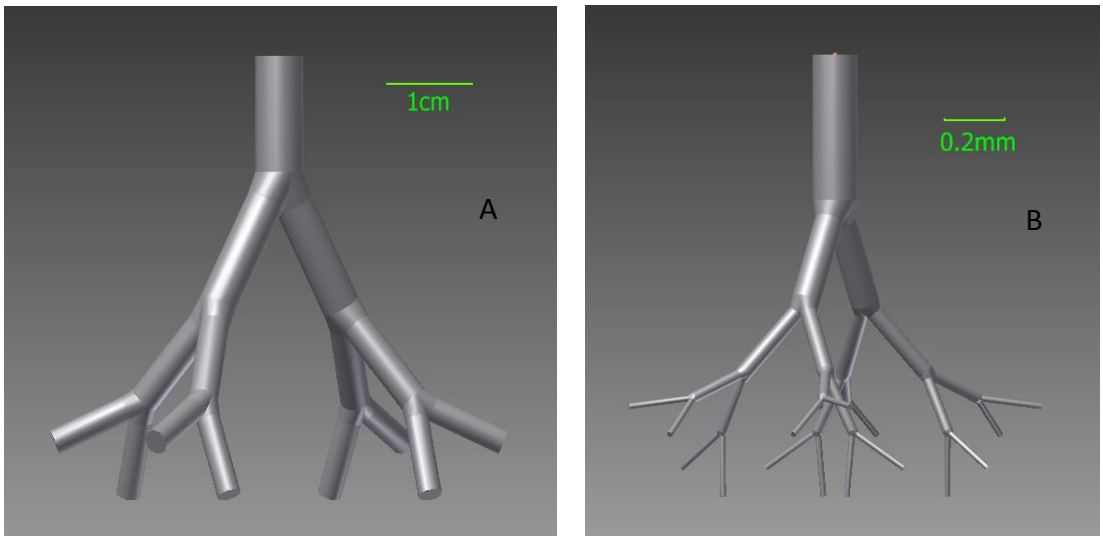

Figure 2.1 Artificial Model, A: artery model; B: vein model

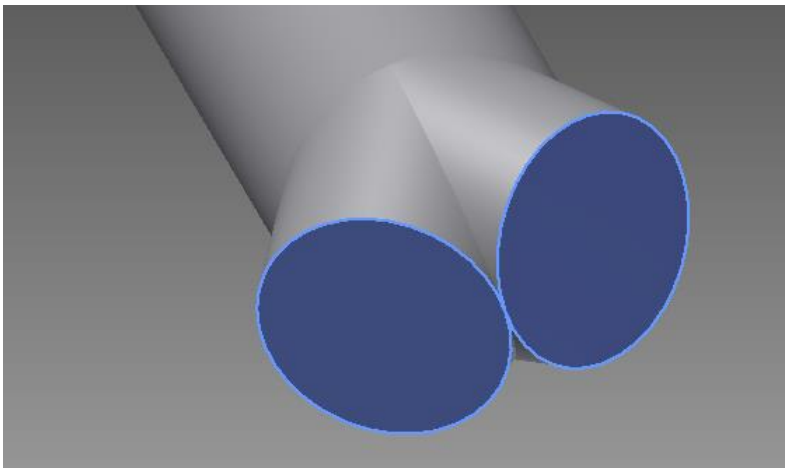

Figure 2.2 3-D view of section close to the bifurcation area of artificial vascular geometry.

	Generation #	Length (mm)	Diameter (mm)
Artificial artery model	1	7.60	5.60
	2	12.70	4.50
	3	10.70	3.50
	4	9.00	2.80

Artificial vein model	1	0.48	0.15
	2	0.31	0.096
	3	0.26	0.056
	4	0.19	0.036
	5	0.20	0.02

Table 2.1 Length and diameter of each branch

2.1.2 Realistic Geometry

In this study, an open source software called VMTK was used to reconstruct the realistic pulmonary geometry. A Magnetic Resonance Imaging (MRI) based Digital Imaging and Communications in Medicine (DICOM) image of a human lung vasculature was imported to VMTK and converted to Visualization Toolkit (VTK) format first. Then a deformable surface was extracted according to the image data and the chosen deformation parameters, as shown in Fig. 2.3. It is a whole lung vascular model, which includes up to 9 generations. It should be noted that because of the large range of branches diameter and grey scale threshold, it is almost impossible to construct the whole vessel in one process. Thus, individual branches are built part by part and merged together later.

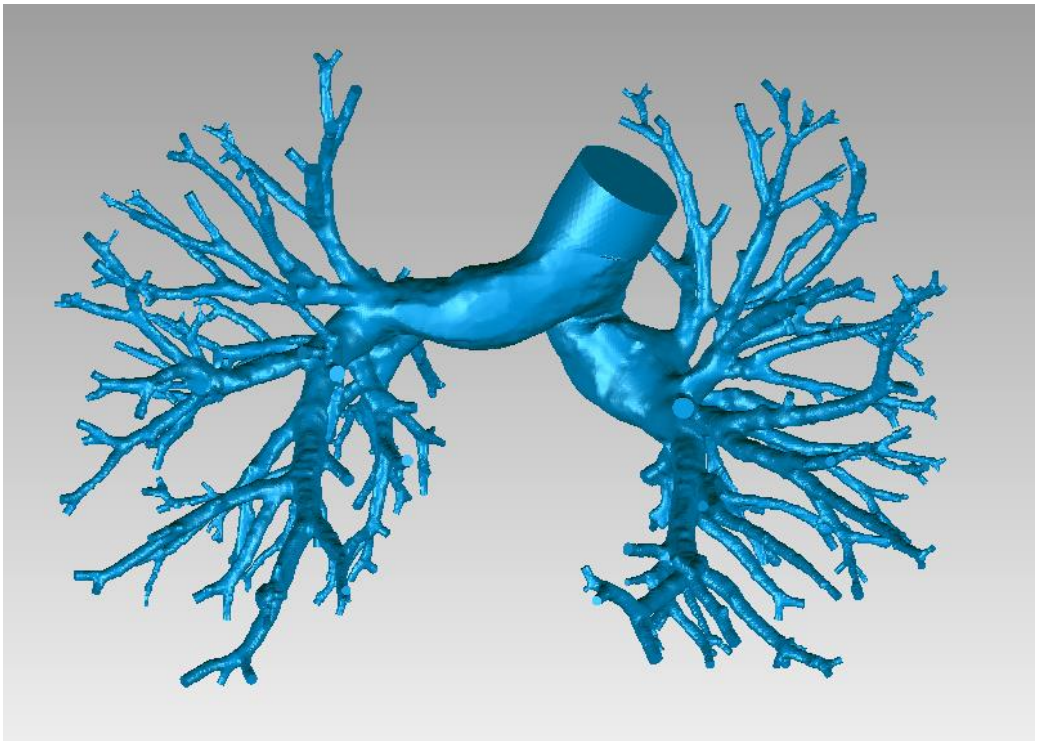

Figure 2.3 Lung vasculature geometry reconstructed from a MRI image, courtesy of Ender A. Finol, Department of Biomedical Engineering, University of Texas San Antonio

Since the model is deformable, it is likely that some outlets are closed with a blobby appearance. Therefore, it is important to clip the blobby endcaps manually. Although, a fully developed parabolic inlet boundary condition has been applied at inlet, to make sure the flow entering and leaving the computational domain is fully developed, flow extensions are added. All the flow extensions are cylinder whose ratio of height to diameter is 2.

It is extremely challenging to model particle delivery in such a complex vascular system that has vessels with diameter from millimeters to centimeters. To develop proper boundary conditions for that is also nontrivial because it has over 200 outlets and is highly asymmetrical. As a first step toward modeling particle delivery in lung vasculature, we select a typical portion of the lung vasculature consisting of 4 generations, as shown in Fig. 2.4A. To illustrate the effects of vascular wall smoothness and characteristic, another model was built as shown in Fig. 2.4B. In this model, coarse surface has been over-smoothed with Geomagic Studio.

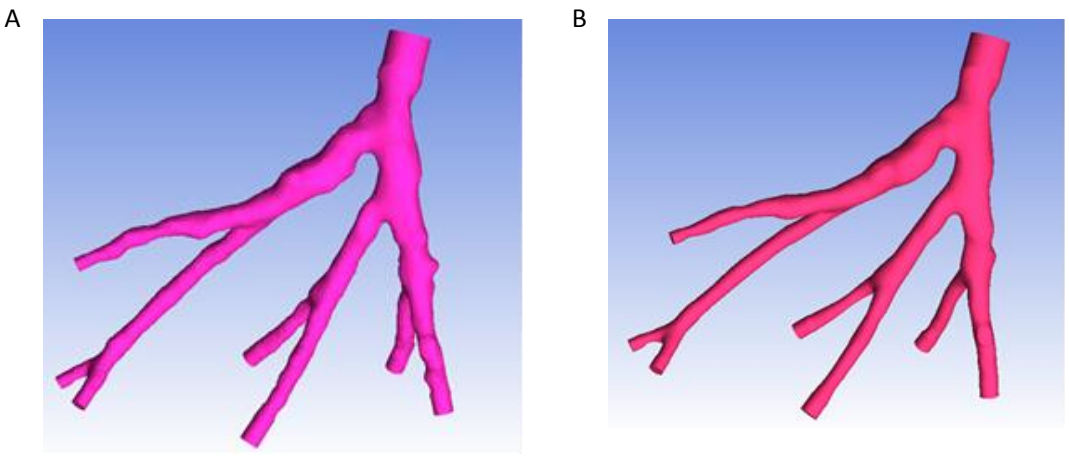

Figure 2.4 Four-generation subunit of pulmonary vascular geometry. (a) is the original subunit; (b) is the over-smoothed subunit

2.2 Mesh

In this study, the mesh model was generated with ICEM-CFD. In order to acquire a better numerical estimation of flow field near vessel's wall and accordingly, carefully track particles, a very small mesh size has been employed near boundaries. To reduce the computation cost of universal small mesh size, a non-uniform mesh is also applied as shown in Fig. 2.5. In this mesh model, size of elements at the center is larger than that of elements near the boundary. Delaunay mesh method [42] was adopted and two prism layers were created near the boundary. The prism layer's initial height is 0.02mm, following exponential growth law with the height ratio of 1.2. The final mesh features about 9.263 million elements. Typical run times for the fluid flow and particles delivery simulation on a 20 processors workstation with parallel algorithm was approximately 10-20 h.

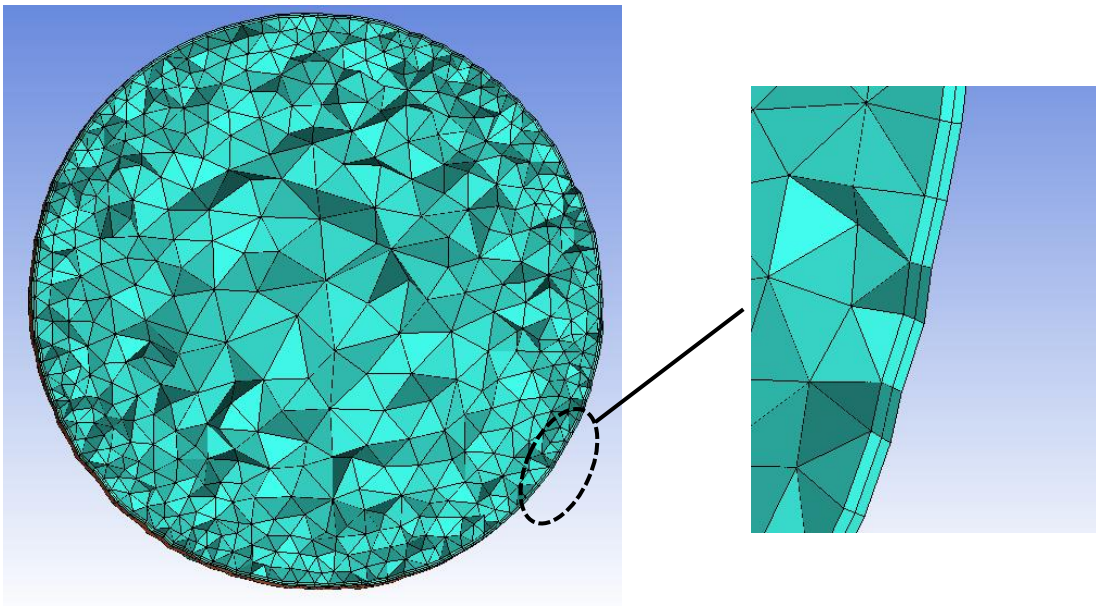

Figure 2.5 A typical mesh over a cross-section of a lung vessel. Mesh size is large in middle and small near boundary.

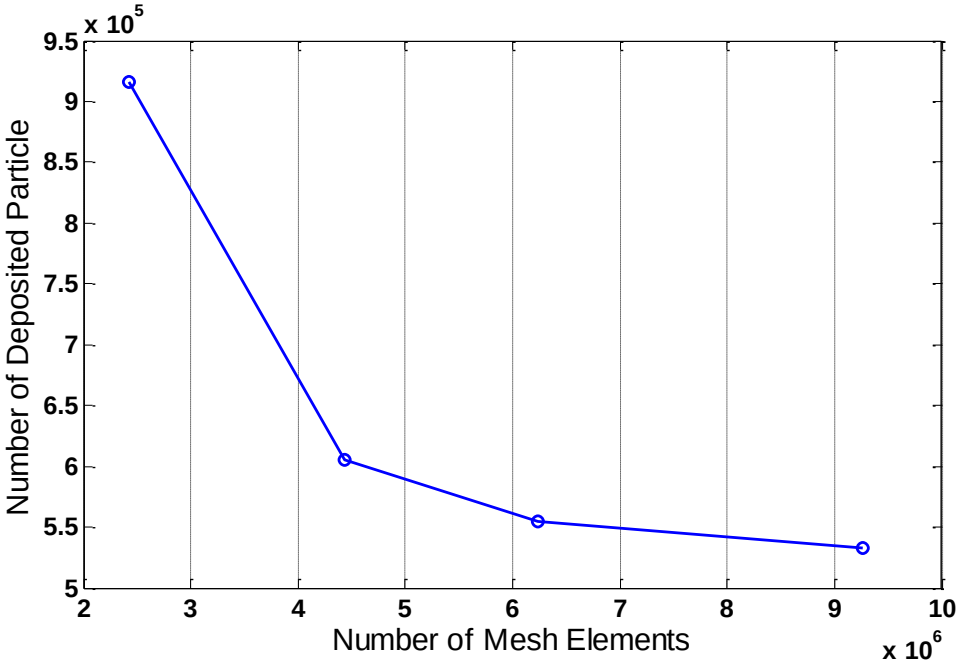

Figure 2.6 Mesh study of particle deposition in the original geometry with pulsatile inlet flow.

To validate the mesh model, models with different mesh sizes (The minimum mesh size limits are 0.2, 0.15, 0.125 and 0.1mm respectively) have been run in a same flow and boundary conditions. The results is shown in Fig. 2.6. The result would not change

when we continue reducing the grid size. To study the different deposition fractions of different vascular parts, the vascular network is divided to different regions, as shown in Fig. 2.7. Each color represents different regions of the lung vasculature, as labeled in Fig. 2.7.

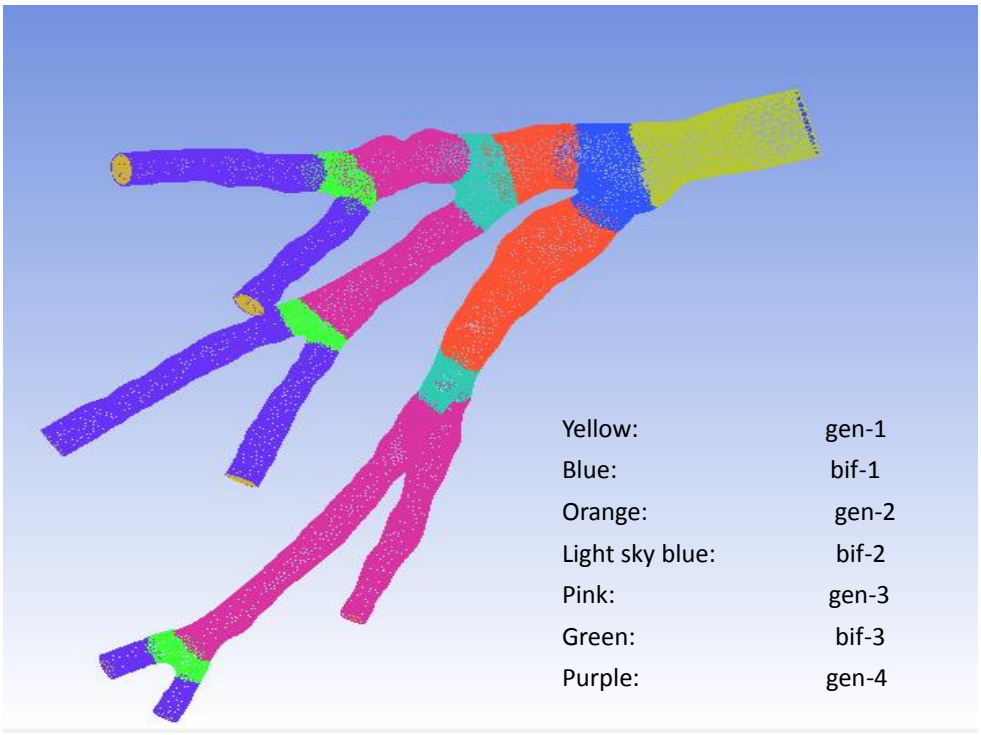

Figure 2.7 Mesh model of lung vasculature split to different regions.(Gen: Generation; Bif: Bifurcation)

2.3 Governing Equations for Blood Flow

In general, blood flow in tapered elastic vessels is pulsatile flow. The fluid is non-Newtonian. Computational fluid dynamics, which requires solving the Navier-Stokes equation, together with appropriate non-Newtonian constitutive relations for blood should be used. It also needs to be coupled with the dynamics of the compliant vessels through which blood flows. But for large arteries, blood can usually be modeled as incompressible and Newtonian [43].

In this study, blood flow is assumed to be laminar and Newtonian. A commercial finite-volume- based CFD solve, Fluent 14.5.0 (ANSYS Inc.) was used for flow

simulation. The blood flow is governed by the Momentum Conservation Equation and Mass Conservation Equation.

$$\frac{\partial}{\partial t}(\rho\vec{v}) + \nabla \cdot (\rho\vec{v}\vec{v}) = -\nabla p + \nabla \cdot (\tau) + \rho\vec{g} + \vec{F} \quad (1)$$

Where p is the static pressure, τ is the stress tensor (described below), $\vec{g}$ and $\vec{F}$ are the gravitational body force and external force, respectively.

The stress tensor τ is given by

$$\tau = \mu[(\nabla\vec{v} + \nabla\vec{v}^T) - \frac{2}{3}\nabla \cdot \vec{v}I] \quad (2)$$

Where μ is the molecular viscosity, I is the unit tensor, and the second term on the right hand side is the effect of volume dilation.

$$\frac{\partial \rho}{\partial t} + \nabla \cdot (\rho\vec{v}) = 0 \quad (3)$$

Eqn. 3 is the general form of the mass conservation equation, or continuity equation and is valid for incompressible as well as compressible flows.

All the blood properties used in this study are summarized in table 2.2

Properties	value
Density	1060kg/m^3
Viscosity	0.003Pa•s
Thermal Conductivity	0.52W/m ℃

Table 2.2 Blood properties

2.4 Governing Equations for Particles Transportation

2.4.1 Particles Tracking

Nanoparticles are delivered to human body by various methods, including inhalation, oral delivery and injection. Among these methods, intravenous injection (IV) is commonly used. After IV, nanoparticles would transport along the blood flow through the vascular network. In common, nanoparticles can be affected by physical

interactions with blood components, in particular with red blood cell. For simplicity of this work, it is assumed that particles transport and distribution are only affected by the blood flow and the interactions with vascular wall.

Trajectory of a discrete phase particle is predicted by integrating the force balance on the particle, which is written in a Lagrangian reference frame. This force balance equates the particle inertia with the forces acting on the particle, and can be expressed as

$$\frac{du_p}{dt} = F_D\left(\vec{u} - \vec{u}_p\right) + \frac{\vec{g}(\rho_p - \rho)}{\rho_p} + \vec{F} \quad (4)$$

Where $\vec{u}$ is the fluid phase velocity, $\vec{u}_p$ is the particle velocity, ρ is the fluid density, ρ_p is the density of the particle, $\vec{F}$ is an additional acceleration term, $F_D\left(\vec{u} - \vec{u}_p\right)$ is the drag force per unit particle mass and

$$F_D = \frac{18\mu}{\rho_p d_p^2 C_c} \quad (5)$$

Here, d_p is the particle diameter, μ is the molecular viscosity of the fluid, C_c is the Cunningham correction factor, which will be mentioned later.

In this study, it is assumed that the density of particle (ρ_p) is the same as density of blood (ρ). Particles are injected with the same time step as the calculation time step of flow from the inlet. In total, 2 million particles are released continuously from inlet for one second. Particles size ranges from 1nm to 500nm with uniform distribution. The particle initial position is also random allocated at the inlet. Trapezoidal and implicit tracking schemes are chosen for higher order and lower order numerical tracking schemes respectively. Tolerance of relative error is set to 10^{-5}, and the maximum number of integration steps is 10^6.

2.4.2 Nanoparticle Brownian Dynamics

Brownian motion describes the random motion of submicron particles which is subjected to the random collisions from the surrounding liquid molecules [44]. To include such effects in this simulation, the Brownian force F_{b_i} is modeled as a

Gaussian white noise process with spectral intensity $S_{n,ij}$ given by

$$S_{n,ij} = S_0 \delta_{ij} \tag{6}$$

Where δ_{ij} is the Kronecker delta function, and

$$S_0 = \frac{216 \upsilon k_B T}{\pi^2 \rho d_p^5 (\frac{\rho_p}{\rho})^2 C_c} \tag{7}$$

T is the absolute temperature of the fluid, υ is the kinematic viscosity, Cc is the Cunningham correction, and k_B is the Boltzmann constant [45].

Cunningham factor is used to correct Stokes' drag law, and can be expressed as

$$\mathrm{Cc} = 1 + \frac{2\lambda}{d_p}(1.257 + 0.4e^{-(1.1 d_p / 2\lambda)}) \tag{8}$$

Where λ is the molecular mean free path. Here, the mean free path λ for blood is assumed as 0, due to the high molecular density. Thus, the Cunningham factor is 1 [46].

Amplitudes of the Brownian force components are defined by

$$F_{b_i} = \zeta_i \sqrt{\frac{\pi S_0}{\Delta t}} \tag{9}$$

Where ζ_i is zero-mean, unit-variance-independent Gaussian random number, and Δt is the calculation time step. The amplitudes of the Brownian force components are evaluated at each time step of simulation.

2.4.3 Saffman Lift Force

Small particles in shear field should experience a lift force perpendicular to the direction of flow. The lift force originates from the inertia effects in the viscous flow around the particle and move particles from higher pressure region to lower pressure region. For sub-micron particles, the Saffman's lift force usually cannot be neglected. The generalized expression of Saffman's lift force is:

$$\vec{F} = \frac{2Kv^{1/2}\rho d_{ij}}{\rho_p d_p (d_{lk} d_{kl})} (\vec{v} - \vec{v}_p) \tag{10}$$

Where K =2.594 and d_{ij} is the deformation tensor.

2.5 Particles Binding Model

In this study, a receptor-ligand model proposed by Decuzzi *et al*. [41] is adopted to calculate the particle deposition probability. The adhesive strength of particles depends on the selective binding of the molecules expressed over the target surface and their counter-molecules conjugated at the particle surface. The dislodge forces are influenced by the other physiological factors as wall shear stress, particle shape and size, as sketched in Fig. 2.8.

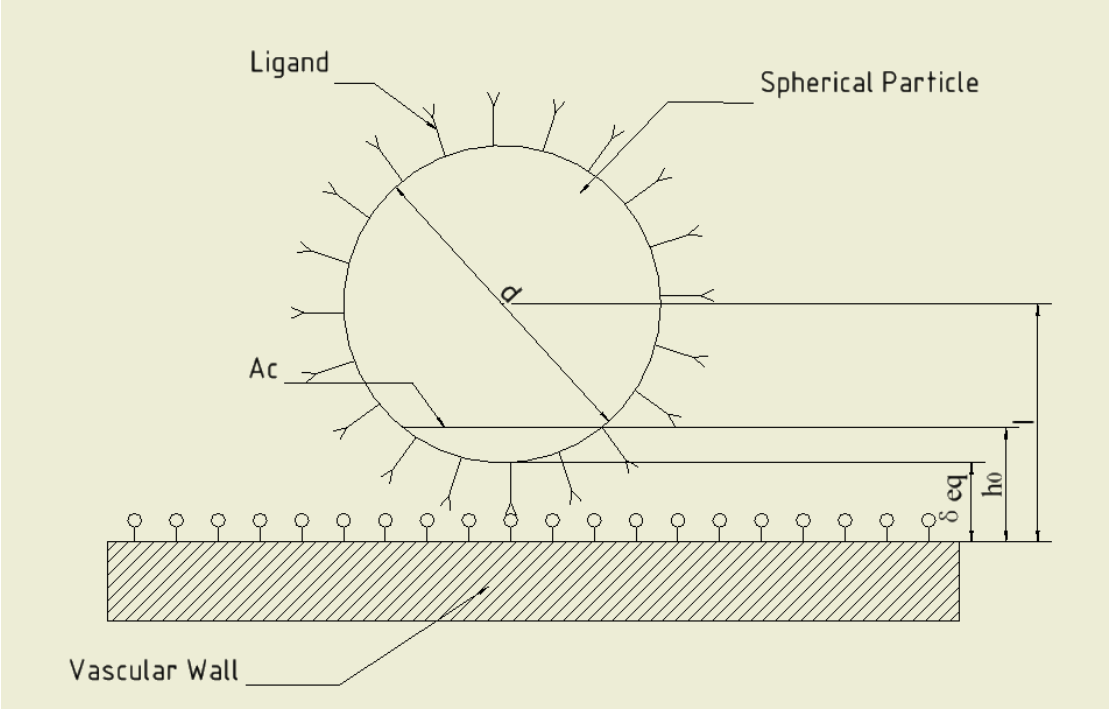

Figure 2.8 Illustration of a spherical particle in specific contact with vascular wall. δ_{eq} is the separation distance between the spheroidal particle and the vascular wall; h_0 is the maximum distance of the spheroidal particle from the vascular wall at which a specific bond can occur; d is the diameter of the particle.

Dislodging forces, the drag force F along the flow direction and the torque T, are affected by the particle size d, separation distance from the vascular wall l and the shear stress μS at the wall. Their explicit expressions are shown as:

$$F = 6\pi l \mu S F^S \tag{11}$$

and

$$T = 0.5\pi d^3 \mu S T^S \tag{12}$$

Where the coefficients, F^S and T^S depend on aspect ratio. Here, F^S=1.668 and T^S=0.944 for sphere particles [47].

When the particle surface and the vascular wall are close enough, the ligands with surface density m_l on the particle and the receptors with surface density m_r on the vascular wall can form bonds stochastically. A probability of adhesion P_a is introduced here, which defined as the probability of having at least one bond formed between the particle and the substrate surface.

$$P_a = m_r m_l K_a^0 A_c \exp[-\frac{\lambda f}{k_B T}] \tag{13}$$

where K_a^0 is the association constant at zero load of the ligand-receptor pair; A_c is the interaction area between the particle and the substrate; f is the force per unit of ligand-receptor; λ is a characteristic length of the ligand-receptor bond; and $k_B T$ is the Boltzman thermal energy.

From Fig. 2.8, A_c can be easily derived as:

$$A_c = 0.25\pi d^2(1 - (1 - \frac{2*(h_0 - \delta_{eq})}{d})^2) \tag{14}$$

f can be expressed as the ratio of total dislodging force F_{dis} and the area of interaction A_c multiplied by the surface density of the receptors, that is $f = F_{dis}/(m_r A_c)$. As usually done, it is assumed that the force F_{dis} is uniformly shared among the bonds; whereas the torque T is only shared uniformly within the bonds which are stretched, thus, for sphere particle,

$$\frac{F_{dis}}{A_c} = \frac{F}{A_c} + \frac{2T}{A_c r_0} = \frac{3\pi d(d/2 + \delta_{eq})\mu S F^S}{A_c} + \pi d^3 \mu S T^S / A_c r_0 \tag{15}$$

Where r_0 is the radius of the interaction surface.

Combining Eqns. (13), (14) and (15), Pa can be expressed as

$$P_a = m_r m_l K_a^0 \pi r_0^2 \exp[-\frac{\lambda d \mu S}{2 k_B T r_0^2 m_r}[6(d/2 + \delta_{eq})F^S + 2\frac{d^2}{r_0}T^S]] \tag{16}$$

In this thesis, the values of parameters are chosen and summarized in table 2.3.

Parameters	value
m_r	10^{14}m^2
λ	10^{-10}m
k_B	1.38×10^{-23}m^{2}kg/s^{2}K

m_r	300K
h_0	10^{-8}
δ_{eq}	5×10^{-9}

Table 2.3 Binding probability parameters

To simplify having realistic and proper values of K_a^0 and m_l for particles with different sizes, we made an assumption that at zero shear stress, the binding probability is assumed to be one. The proper values of K_a^0 and m_l depends on particle type of ligand-receptor used and local chemical conditions, and usually requires complex experimental tests on particle binding dynamics. To simply this process and make our results applicable to delivery of general types of particles, we normalized the particle binding probability under a range of shear stress to that under zero shear stress. In another word, the binding probability is assumed to be one at zero shear stress, which is reasonable according to experimental observations. The particle binding probability for different particle size exposed to various dislodging shear stress is shown in Fig. 2.9.

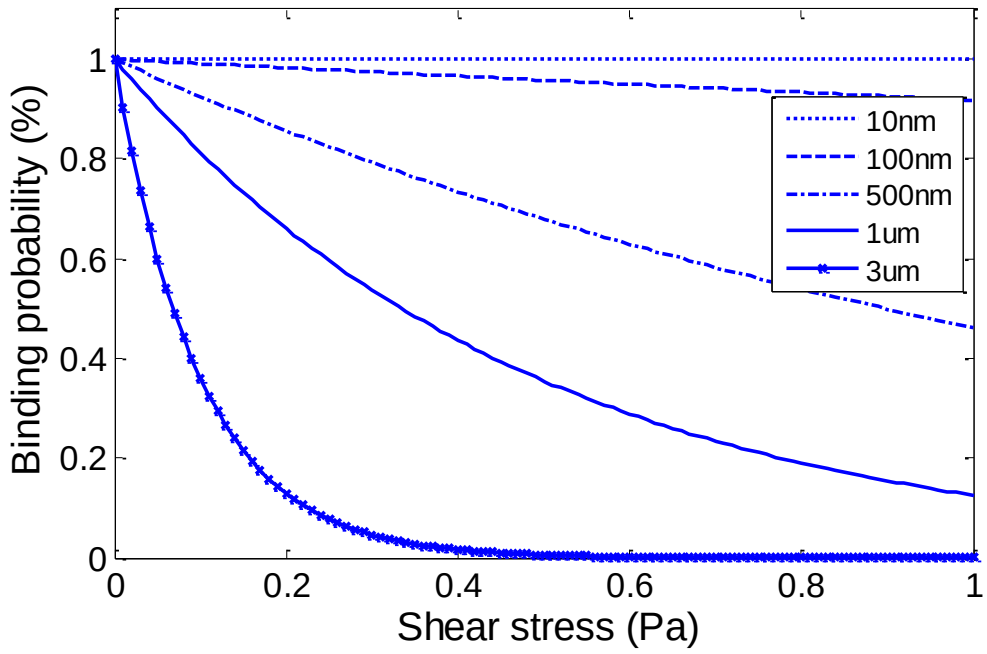

Figure 2.9 Binding probabilities for particles of different size (10nm, 100nm, 500nm, 1μm and 3μm) under a range of shear stresses.

2.6 Boundary Condition

2.6.1 Inlet Velocity Profile

The blood flow in pulmonary arteries is pulsatile. As shown in (Fig 2 of reference [48]), the flow patterns in the pulmonary vasculature of normal subjects showed no retrograde flow during diastole. Furthermore, there was no apparent difference between the flow profiles of right and left pulmonary arteries in these subjects which can be interpreted into more or less equal perfusion for both vascular beds. As mentioned before, just a small portion of realistic human left pulmonary vasculature has been used for modeling particle transport and deposition. Thus, the appropriate inlet velocity into this model structure has to be carefully calculated. For this purpose, experimentally measured cardiac flow to left pulmonary artery along with morphometric data of human pulmonary vasculature is used in this study [48]. The approximate number and diameter of vessels in every generation can be extracted from this data set. Using inlet surface area, the appropriate number of vessels in that specific generation can be interpolated. Subsequently, the inlet flow rate into our reference geometry can be calculated. In order to employ experimentally measured left pulmonary artery data points in our simulation, least square method is utilized to determine coefficients of Fourier series expansion. Moreover, fully developed flow assumption is used for the inlet velocity profile in order to eradicate unrealistic effect of developing region on simulation results. Thus, inlet profile will have a parabolic outline which is changing with time during cardiac cycle as shown in Fig. 2.10.

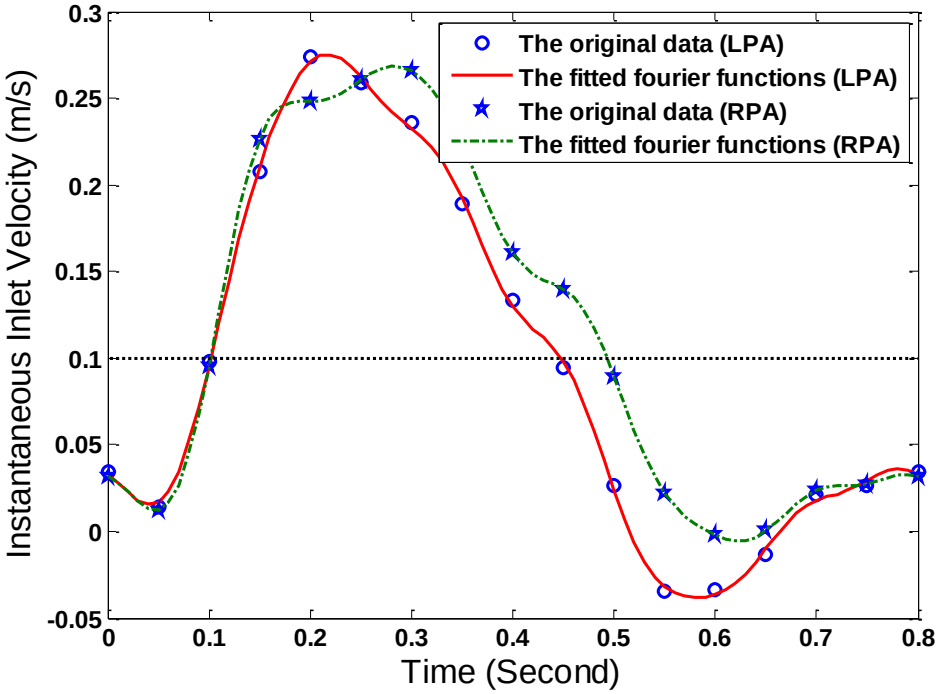

Figure 2.10 Instantaneous inlet velocity of pulmonary artery.

2.6.2 Outlet Boundary Condition

Using Strahler's ordering system [49], Kassab *et al*. [50] defined every vessel between two successive bifurcation points as a segment. Moreover, they identified vascular element as a set of segments of the same order connected in series from the inlet to the outlet of the arterial tree. The segment length is the distance between bifurcation points. The diameter of an element was computed as the average of the diameters of the segments that make up the element. Similarly, the length of an element was obtained by adding the lengths of the segments within that specific element. Moreover, Huang *et al.* [51], in their morphometric study of human pulmonary arteries, introduced a matrix that characterizes the connectivity of lung arteries. In this matrix, C(m,n) is the ratio of the number of order m elements, evolving directly from order n elements, to the total number of order n elements. This connectivity matrix and statistical data set were derived for a human left pulmonary vasculature. Furthermore, flow circuits can be built of elements because segments are already connected in series. Thus, we can develop a code to generate a tree of pulmonary elements using

connectivity information of pulmonary elements for deriving the overall resistance at each outlet of our image-based model structure. The smallest vessels in this data set have a diameter of 20 μm, slightly larger than capillaries. It should also be mentioned that the outlets of this morphometry-based tree, the order 1 elements, were modeled as emptying into a reservoir with relative zero pressure. Furthermore, the dynamic viscosity was set to 0.04 poise except in vessels of order 1, 2, and 3, where the values were assumed to be 0.025, 0.03, and 0.035 poise, respectively, to account for the reduced apparent viscosity in lumens with small diameters [52]. Finally, the overall resistances at the beginning of every generation have been calculated as shown in Fig. 2.11. Thus, during CFD solving procedure, the outlet pressure will be updated at every iteration using volumetric outflow and downstream calculated resistance. Here, in our model, generation order of downstream vessel may vary from 8 to 12, see Fig. 2.11.

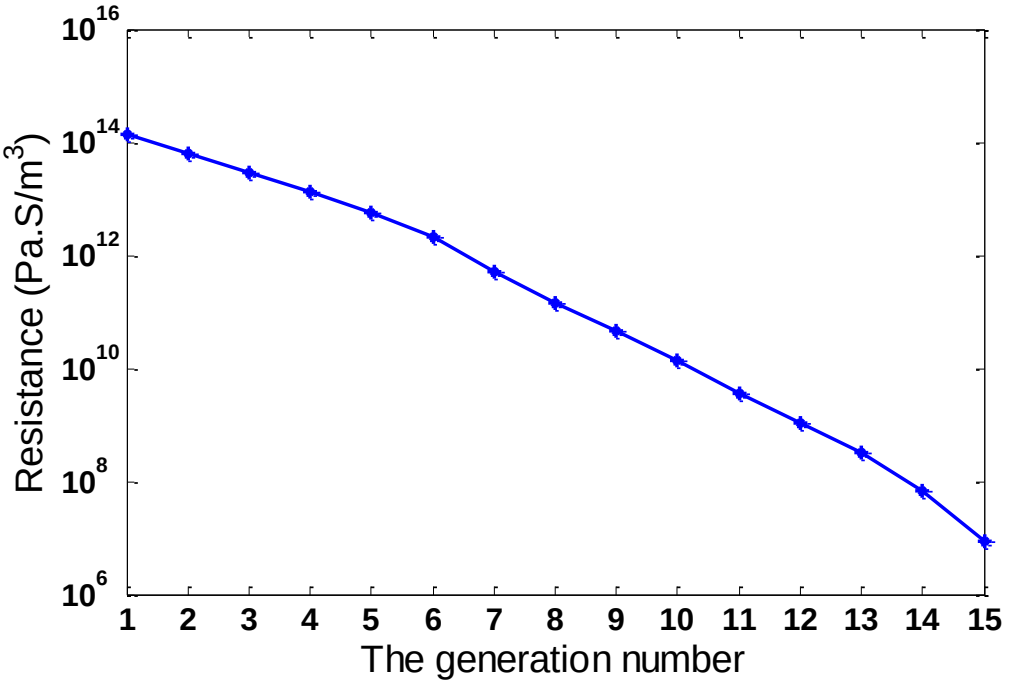

Figure 2.11 The overall resistances at the beginning of every generation of vascular network. Out model ranges from 8th to 12th.generation

Chapter 3

Result and Discussion

In the following section, the results of particle tracking simulation in lung vasculature are presented and discussed in detail. It should be mentioned that the entrance effect on modeling results was minimized by adding flow extensions and fully developed inlet flow profile, and unless otherwise stated, all the results of artificial geometry are referred to artificial artery model. Small size artificial vein model is only used to do a comparison and verify the CFD method. Furthermore, since available surface areas for particle binding in artificial and realistic model structures are different, some results have been normalized with the corresponding surface area.

3.1 Steady State flow

Steady inlet velocities within physiological range of 0.05 to 0.2 m/s have been chosen to compare particle deposition with respect to particle diameter size. For this purpose, 2 million particles of different sizes in uniform distribution have been injected into original geometry model with steady state flow condition. The results are listed in Fig. 3.1A and Fig. 3.1B in two different ranges of particle diameters. As depicted in Fig. 3.1A, particles have higher deposition fraction under inlet velocity of 0.15 m/s than that under other inlet velocity in majority of diameters. Furthermore, since diffusion mechanism is the dominant driving force of small size particles in low flow rate region, particles with diameters less than 20 nm have the highest deposition percentages in 0.05 m/s inlet velocity case, see Fig. 3.1A. As mentioned before, the particle binding probability would decrease by increasing shear stress and particle size, as illustrated in Fig. 2.9. It is depicted in Fig. 3.1B that the binding fraction will gradually decrease as particle diameter increases. Furthermore, this decrease is also intensified by increasing luminal flow rate due to decreased particle binding probability with increased shear

stress. This phenomenon is consistent with the particle Brownian motion speed in blood, as shown in Fig. 3.2. Particles with diameters less than 20nm have relatively higher Brownian motion speed. Particle displacement decreases dramatically with the increased particle size at the beginning, and then decrease slowly after 20nm.

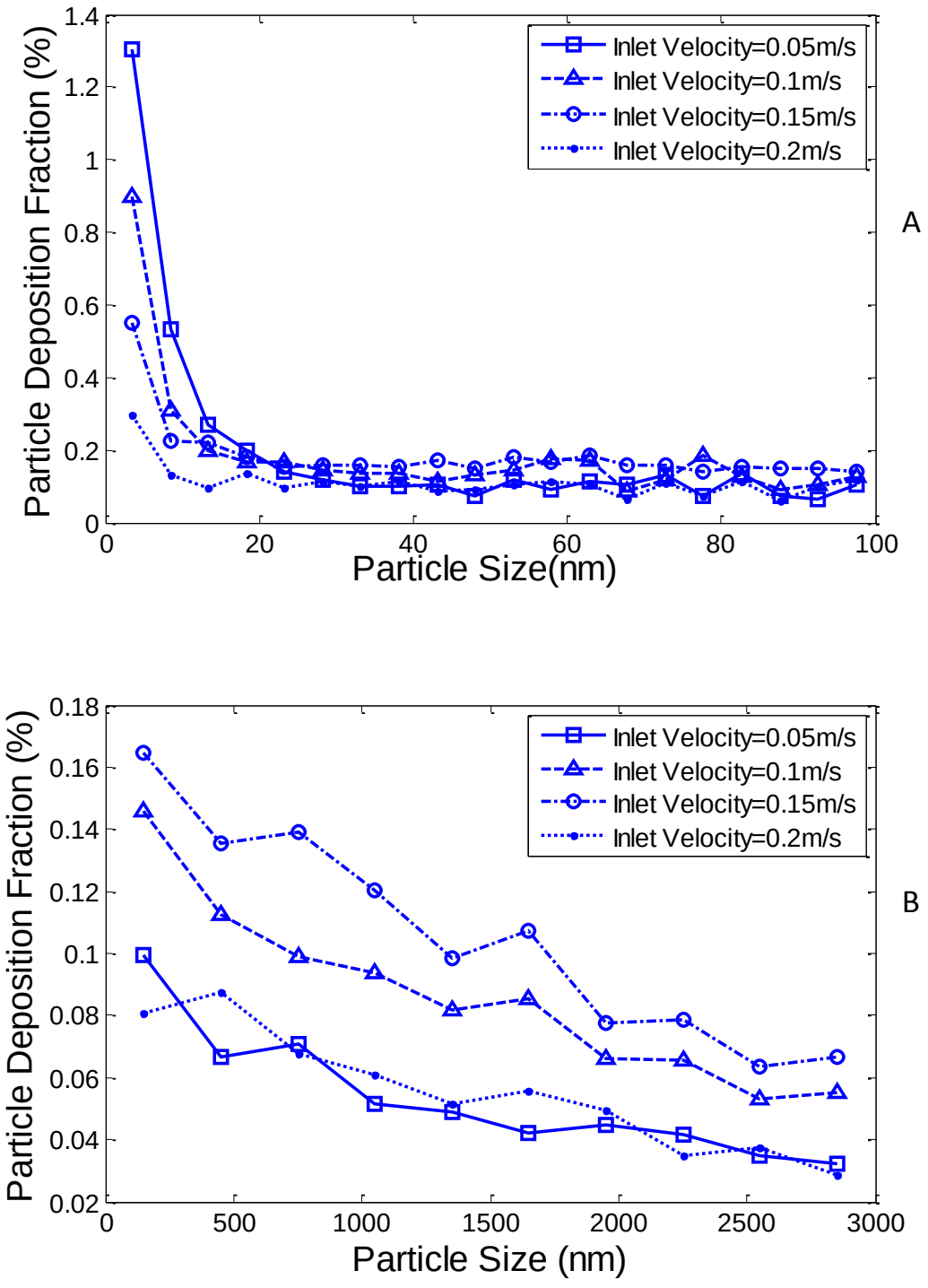

Figure 3.1 Comparing particle deposition fraction at two different ranges of particle

sizes under various steady flow rates: A. 1 to 100nm, B. 1nm to 3μm

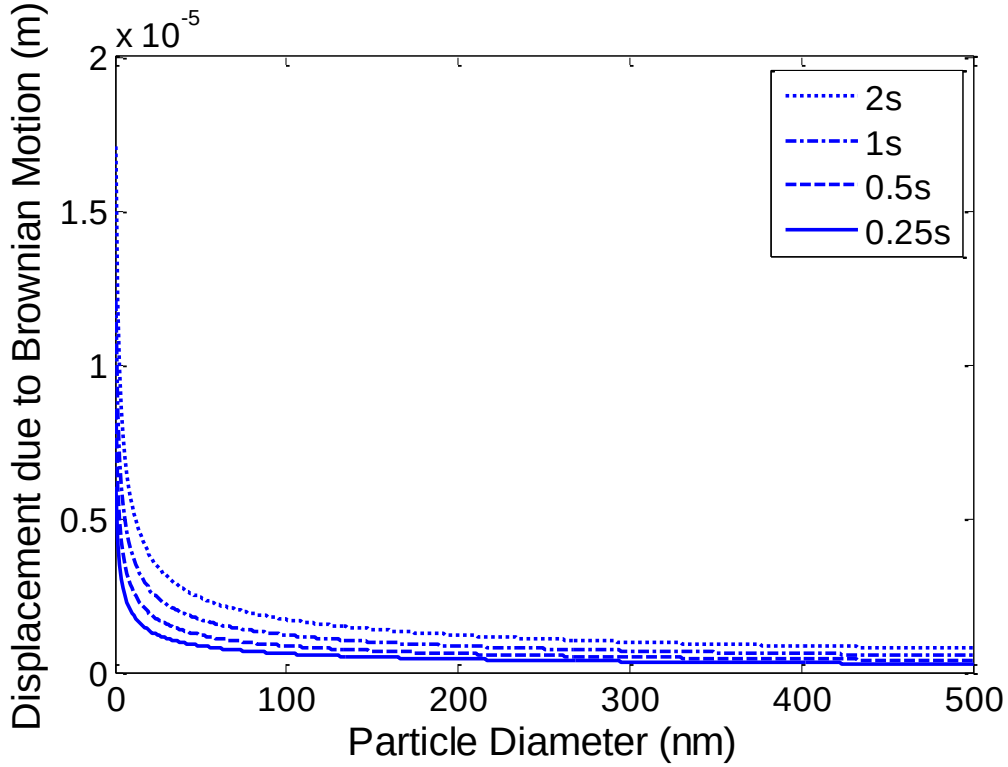

Figure 3.2 Displacement of particles with different sizes due to Brownian motion in different time periods.

To investigate the effect of fluid flow field on particle binding pattern, particle deposition fraction has been studied in original, over-smoothed and artificial Weibel geometry under a steady state flow velocity of 0.1 m/s. It should be noted that the main difference between the original and the over-smoothed model structures is the smoothness of vessel's surface. As shown in Fig. 3.3, the percentage of bound particles is lowest for artificial geometry and highest for original geometry. Due to numerous surface imperfections in realistic model of lung vasculature, streamlines which start at the central regions of inlet surface (accordingly particles carried by them) have higher chance to get closer to the vessel's wall and deposit. In other words, streamlines are more disturbed and fluid mixing is better in realistic vasculature. Thus, the deposition fraction is also influenced by surface smoothness. Hence our realistic geometry is significantly more favorable for particle binding compared to an ideal artificial geometry.

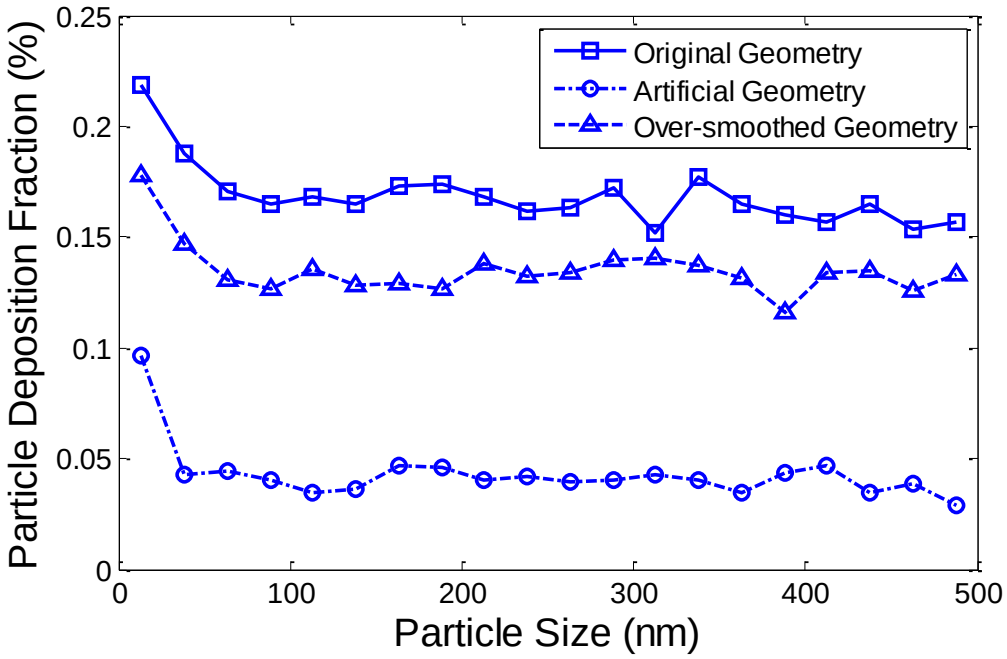

Figure 3.3 Particle deposition fraction using original, over-smoothed and artificial geometry with the same inlet flow rate.

3.2 Pulsatile Flow

Ten million particles with diameters ranging from 1 nm to 3 micron are released into the original geometry under a pulsatile inlet flow profile described in Fig. 2.10. The result for the deposition fraction of particles in various diameters is depicted in the Fig. 3.4A and Fig. 3.4B in two distinct extents of particle size. Moreover, binding distribution pattern of particles in steady flow condition is also added to these figures for comparison purposes. It should be noted again that the average inlet velocity during cardiac cycle is approximately 0.1 m/s, which is chosen for the steady case. As shown in Fig. 3.4A, for smaller particles, binding percentage is noticeably higher when particles are released in pulsatile flow stream because the fluid mixing can be considerably enhanced by unsteady flow. However, as diameter increases, particles deposition fraction decreases significantly because bigger particles would experience more detachment force during peak velocity time period and accordingly, can be easily dislodged from vessel's wall. Consequently, they will have lower chance of successfully

depositing on vessel's wall.

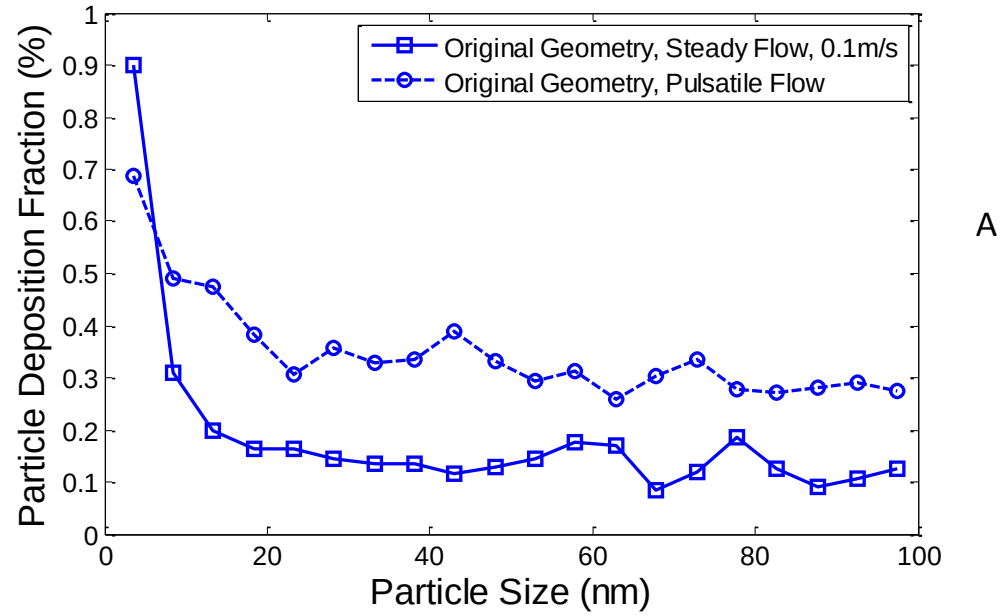

A

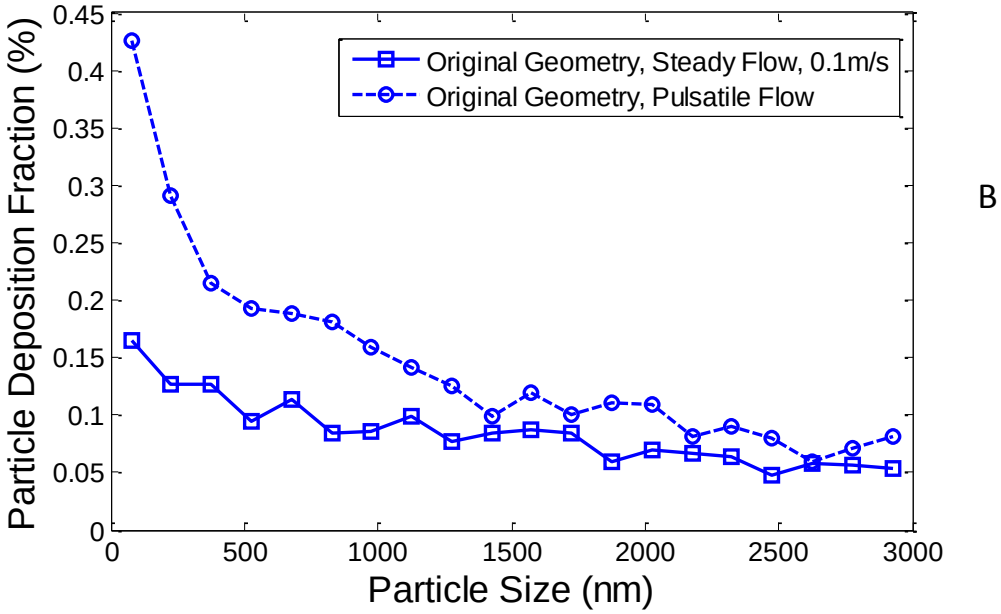

B

Figure 3.4 Particle deposition fraction for particles of different sizes under steady and pulsatile blood flow. For better presentation, is demonstrated at two different particle diameter ranges A. 1 to 100nm, B. 1nm to 3μm

Previously, it has been shown that the artificial geometry has the lowest binding fraction in steady flow condition. But the situation is different when pulsatile inlet flow

condition is applied. It can be observed from Fig. 3.5 that original geometry has the higher deposition rate than over-smoothed and artificial geometries. Furthermore, deposition fraction of particles with diameter less than 20nm is higher for over-smoothed geometry in comparison with artificial geometry results. But for bigger particles, artificial geometry has slightly higher binding rate. Comparing Fig 3.3 to Fig 3.5, it can be found that the particle deposition fraction in artificial geometry increase a lot under pulsatile flow condition. The particle deposition fractions in the other two geometries do increase some, but not as much as that in artificial geometry, which shows the influence of pulsatile flow on regular artificial geometry is stronger than that on complex realistic geometry. It is easy to understand because the complex structure of realistic geometry has already make the fluid flow better mixed than that in regular geometry under steady inlet flow condition. Thus, the enhancement of pulsatile flow on particle deposition fraction to realistic geometry is less than that to regular geometry.

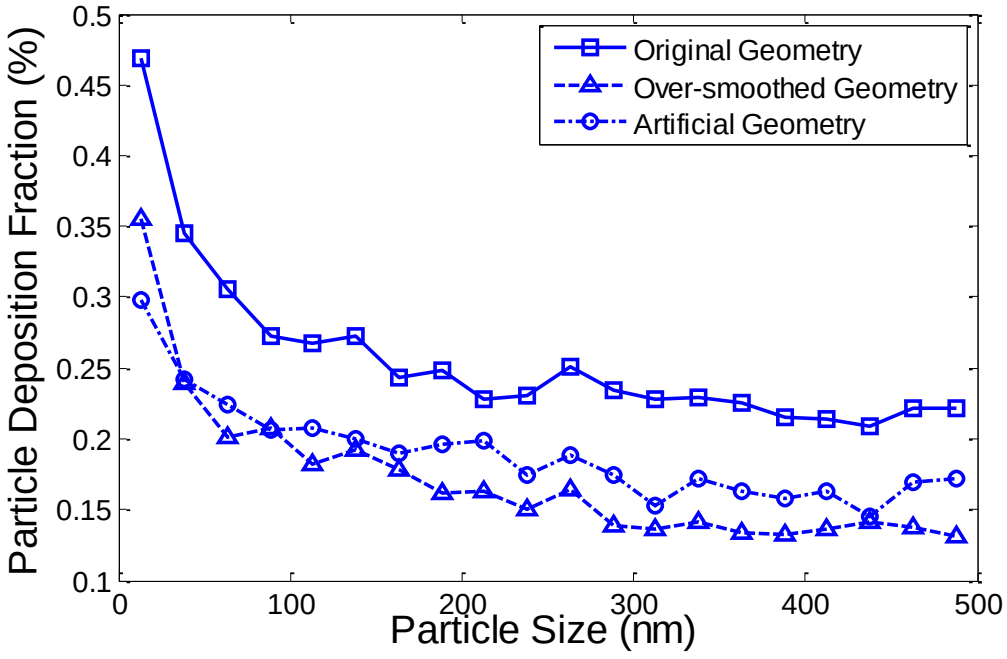

Figure 3.5 Effect of vessel surface smoothness on particle deposition fraction under pulsatile flow condition

Cumulative profiles of particle deposition with respect to time are demonstrated for different simulations in which two million particles with diameters ranging from 1

nm to 0.5 μm are released in original geometry. It is also worthy to mention that particles are injected into pulsatile flow from 0.2s, peak of cardiac inlet velocity, in order to make sure the numerical solution for fluid field is converged and stable and also to eradicate early stage reverse flow effect on results. All profiles are normalized with respect to the total number of deposited particles in that specific simulation. Thus, their ultimate value would be one. Comparing results of steady cases, the deposition process finished faster in higher inlet velocities. The reason is that particles would move and leave lung vasculature faster in higher velocities. Thus, there won't be more particles depositing on vessel's wall after a certain period of time, see Fig. 3.6A.

The blood traveling time through vasculature is approximately same for the case of pulsatile flow and 0.1 m/s steady velocity for both geometries (original and artificial). But as depicted in Fig. 3.6A, particles bind much faster in pulsatile flow even though they have 0.2s lag in their injection time. Moreover, it is observed that particles deposited more rapidly in artificial geometry.

Furthermore, instantaneous binding pattern of trapped particles is analyzed. The instantaneous number of particles deposited in each time interval for realistic cardiac flow in different geometries is derived and shown in Fig. 3.6B. By over smoothing luminal surface imperfections, we won't be able to observe periodic particle binding pattern over time anymore. This feature is amplified for artificial model structure in which a peak of instantaneous deposition happens at the second pulsatile cycle.

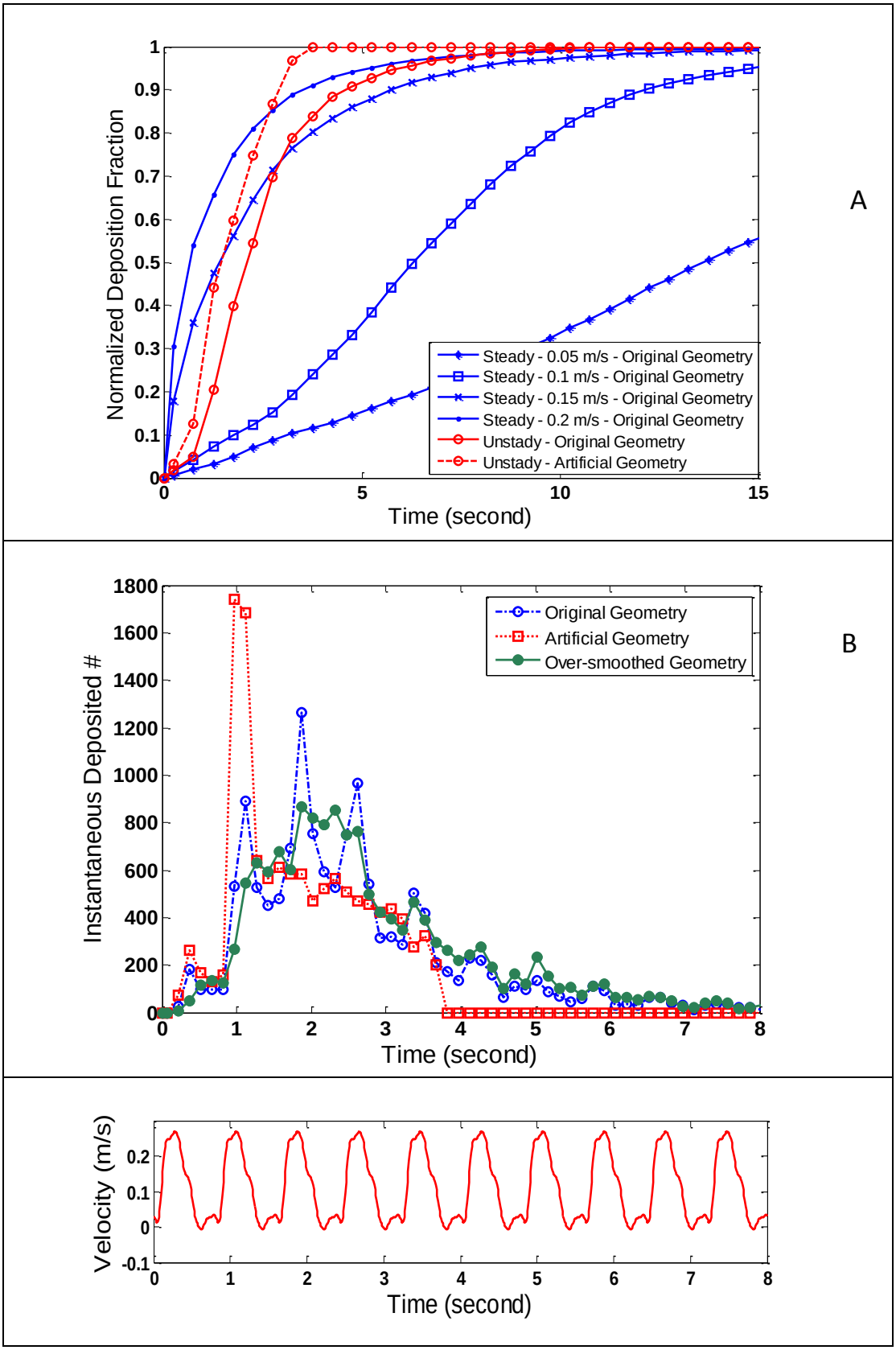
A
Normalized Deposition Fraction
Time (second)
Steady - 0.05 m/s - Original Geometry
Steady - 0.1 m/s - Original Geometry
Steady - 0.15 m/s - Original Geometry
Steady - 0.2 m/s - Original Geometry
Unstady - Original Geometry
Unstady - Artificial Geometry
B
Instantaneous Deposited #
Time (second)
Original Geometry
Artificial Geometry
Over-smoothed Geometry
Velocity (m/s)
Time (second)

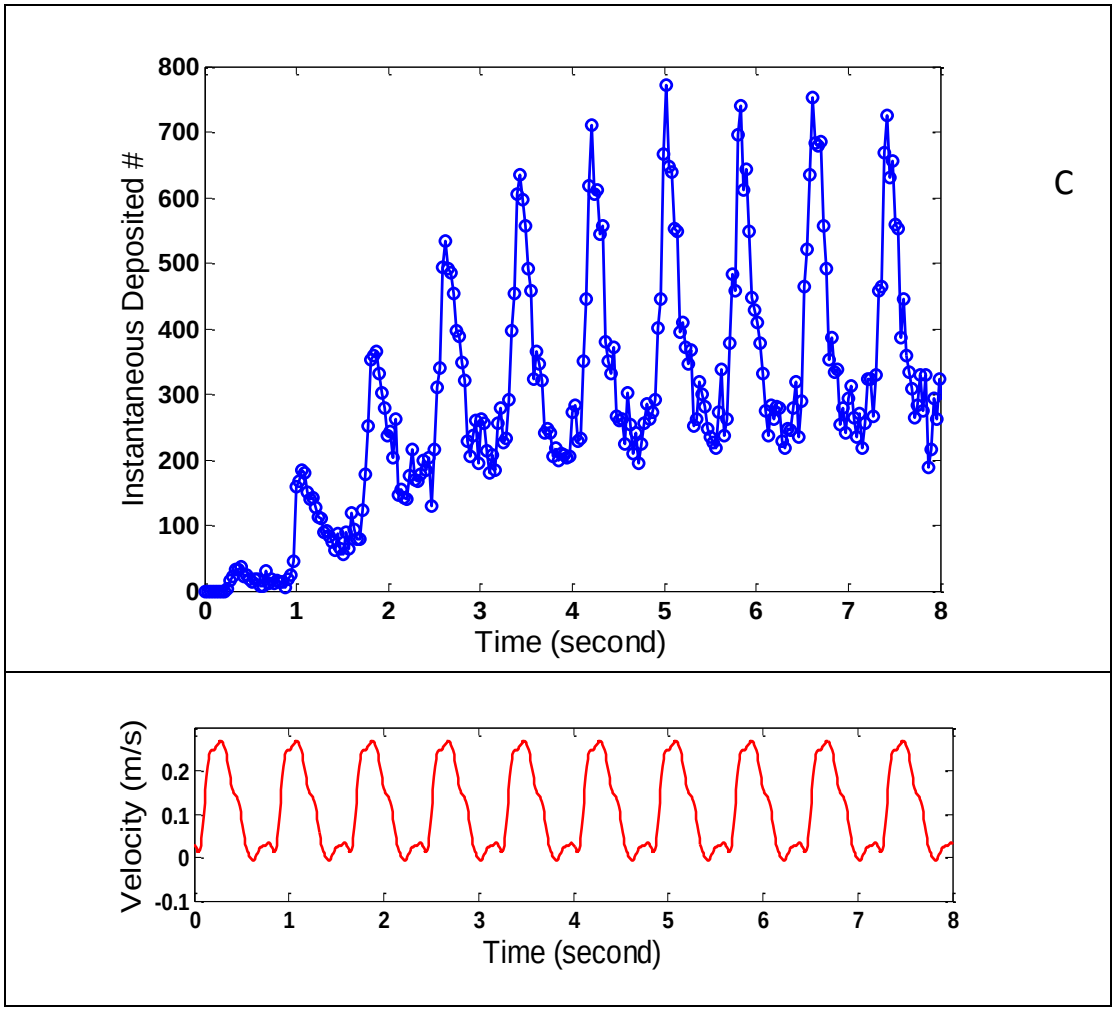

Figure 3.6 Illustrations of deposition profile vs. time for various simulation parameters. A. Cumulative profiles of particle binding in different geometries and flow conditions. B. Instantaneous deposition profile of cardiac flow in geometries with different surface smoothness. C. Instantaneous profile of continuous particle injection in original geometry.

Furthermore, a simulation with continuous injection of particles (1 million per second) into the original geometry was also undertaken to demonstrate the time history of particle deposition better, as shown in Fig. 3.6C. Previously, it was shown that 0.1m/s inlet condition has the highest deposition rate in steady state flow. But here in pulsatile pulmonary flow, it is observed that the peak of deposition rates mainly happens when the flow rate is maximal and accordingly almost no noticeable lag between these occurrences can be detected. Since this pattern is more discernible in the original geometry (Fig. 3.6B), higher particle velocity, better fluid mixing and the presence of stronger vortices in these luminal imperfections can attribute to this phenomenon.

3.3 Deposition Pattern

To better understand the particle deposition pattern, the deposited location of particles are shown in three dimensions for original and artificial geometries in Fig. 3.7. It is observed that the particle deposition density is higher near bifurcation sections of the vasculature network in both original and artificial geometries. It can also be observed in artificial geometry that particles in luminal section of order 3 vessels have higher binding rate. All these phenomena can be explained by the blood flow field. As shown in Fig. 3.8, flow velocity is higher in the middle of the luminal section in steady case, but in unsteady case, higher velocity filed moves to the boundary because of the pulsatile flow field. Under the influence of Saffman lift force, particles are forced to move from high pressure (low tangential velocity) area to low pressure (high tangential velocity). Thus, more particles concentrate in those areas, which makes higher particle deposition fraction there.

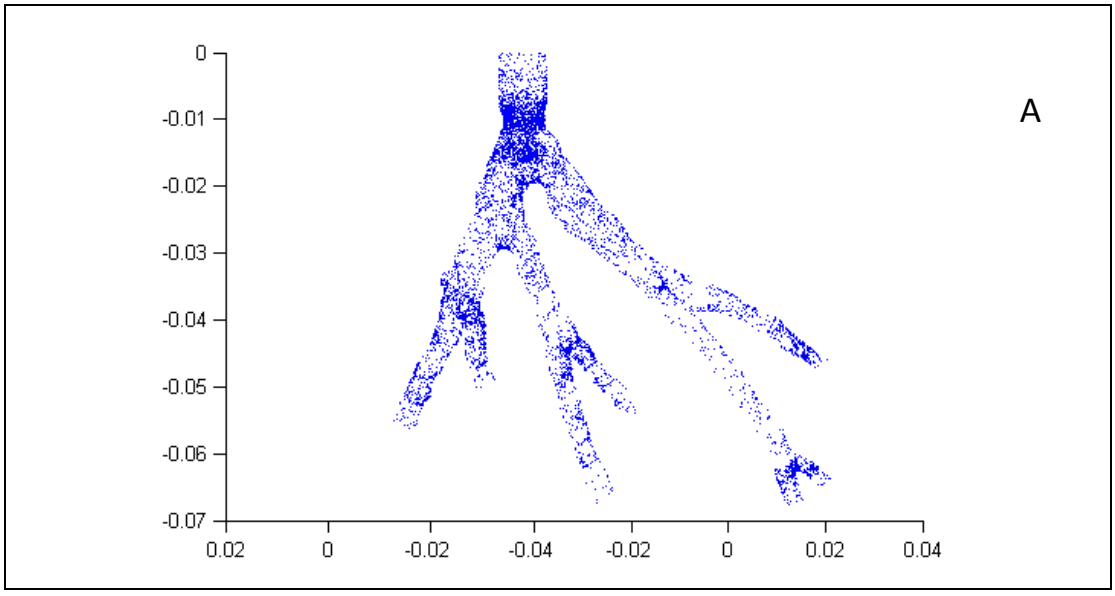

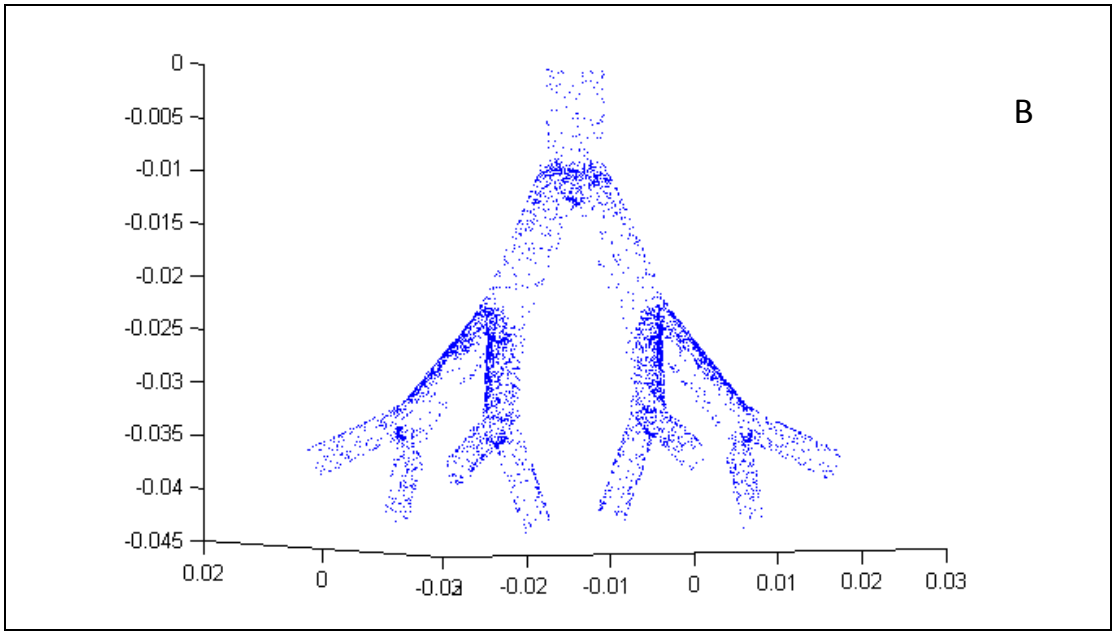

Figure 3.7 3-D demonstration of deposition pattern when releasing 2 million particles with diameter ranging from 1nm to 0.5 μm under pulsatile inlet flow in A. Original lung vascular geometry and B. Artificial Weibel geometry.

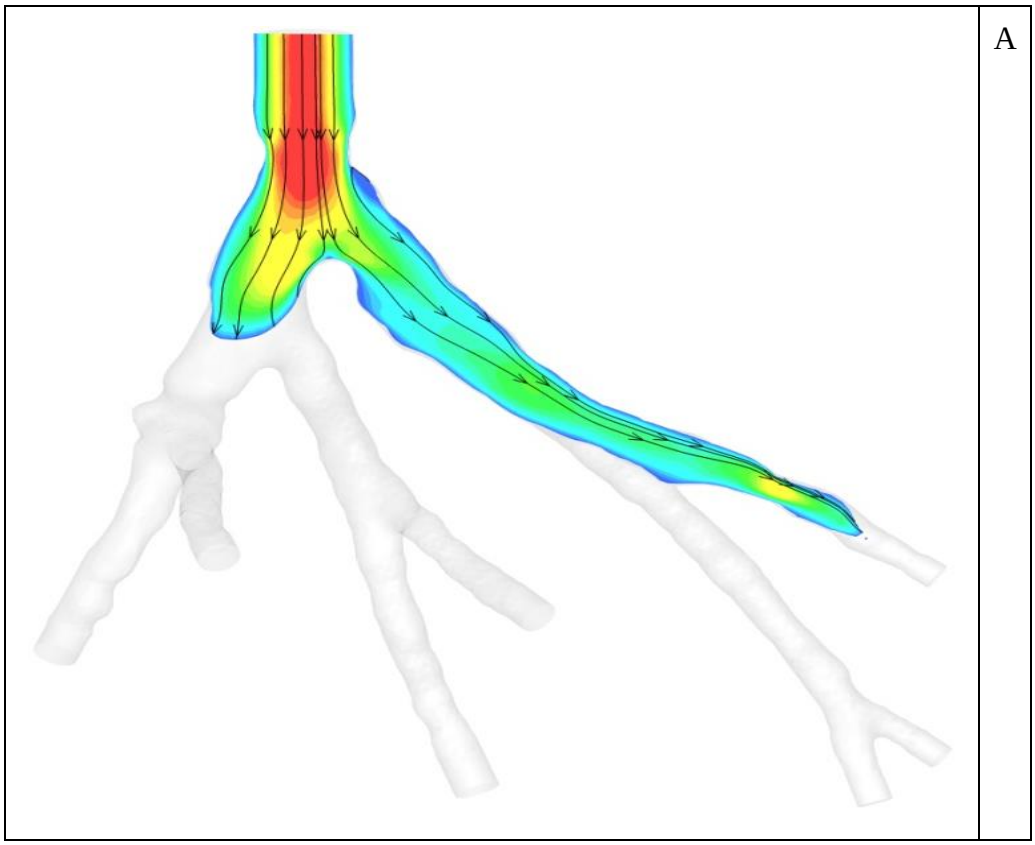

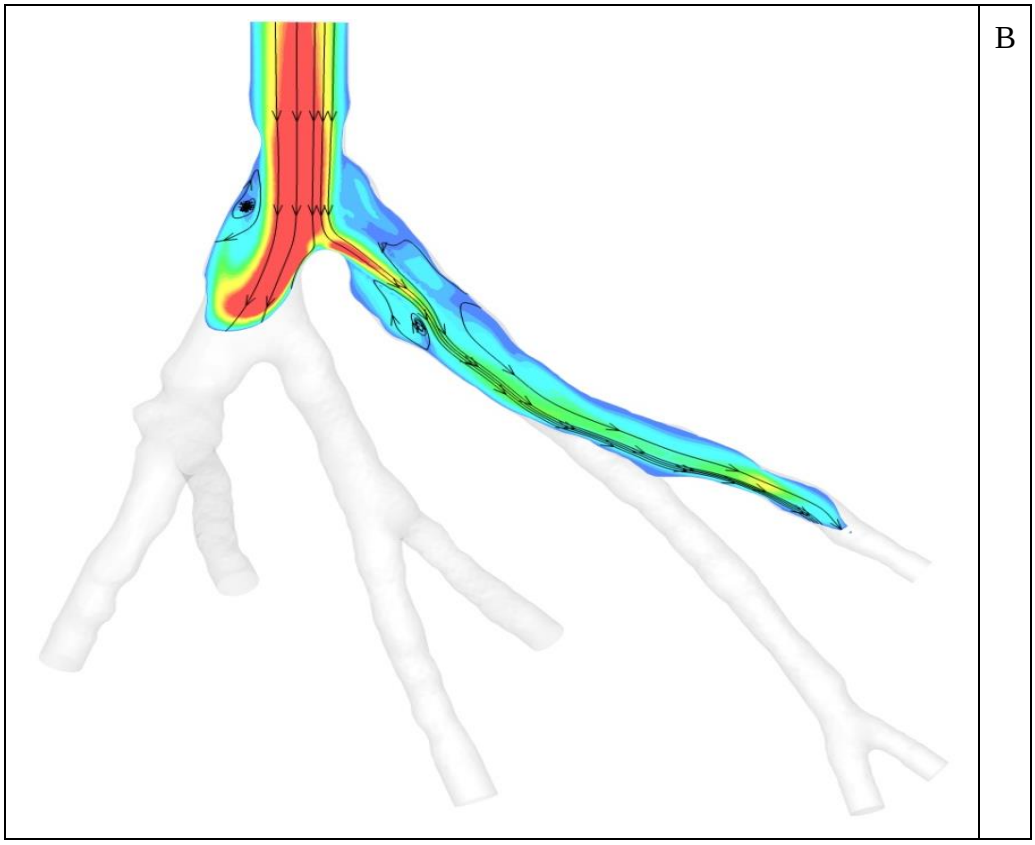

Figure 3.8 Fluid velocity vector in unsteady case and steady case. A: fluid velocity vector of in unsteady case at the time of 0.45s. B: fluid velocity vector in steady case.

In Fig. 3.9, the particle deposition density of the corresponding vasculature it is injected into is shown for steady and unsteady cases. It should also be noted that 2 million particles with size ranging from 1nm to 0.5μm are injected into original geometry for both steady and pulsatile simulations. With much less streamline disturbance due to steady flow, particle deposition density in the first generation is the lowest for steady case. Particle deposition density is approximately uniform throughout all sections in steady flow, see Fig. 3.9A.

In contrast, at the entrance of original geometry in unsteady case, since fluid mixing is enhanced when coupling with surface imperfections, a larger numbers of particles deposit in the first generation. Furthermore, deposited densities at bifurcation sites are considerably higher than that of luminal parts for pulsatile case as shown in Fig. 3.9B. Particle deposition density also increase by generation order, which indicates that particles can transport and deposit in later generations under unsteady flow compared to steady flow. And, to check whether the particle deposition pattern would shift in

much smaller vessels, another case with smaller size artificial vein geometry has been studied. This geometry has the same structure with previous artificial weibel geometry, but different size (branch diameters range from 0.02mm to 0.15mm). The result of this artificial vein model under steady state case is shown in Fig. 3.10. It can be found that the particle deposition density is dramatically increased and particles are more easily to deposit at beginning parts. But, for later parts, the deposition density of particles shows the similar pattern with that in large scale model.

For studying whether particle sizes will influence topographical distribution pattern, the number of deposited particles have been normalized with respect to their target vasculature surface area as well as total number of deposited particles within that diameter range. Using this technique, it is observed that small size particles have higher binding rate at the entrance region, see Fig. 3.11. Moreover, in contrast to particle deposition in respiratory system in which there can be found a specific correlation between the size of particle and the generation order [32], no clear correlation is observed in lung vasculature. Furthermore, it should also be mentioned that particle binding distribution in over-smoothed geometry also have the same feature as original one, but with the lower mass density. But, for artificial vein model, as shown in Fig. 3.12, it can be found that most of deposited particles are those in the range of 1-50nm, but for larger particles, the deposition number is almost zero. These results also proves that Saffman lift force moves particles to some areas of higher tangential velocity when flow rate is high, and because of the high viscosity and weak particle Brownian motion in blood, only when flow rate is very low (0.0176m/s in our artificial vein model), Brownian motion shows dominant influence on deposition process.

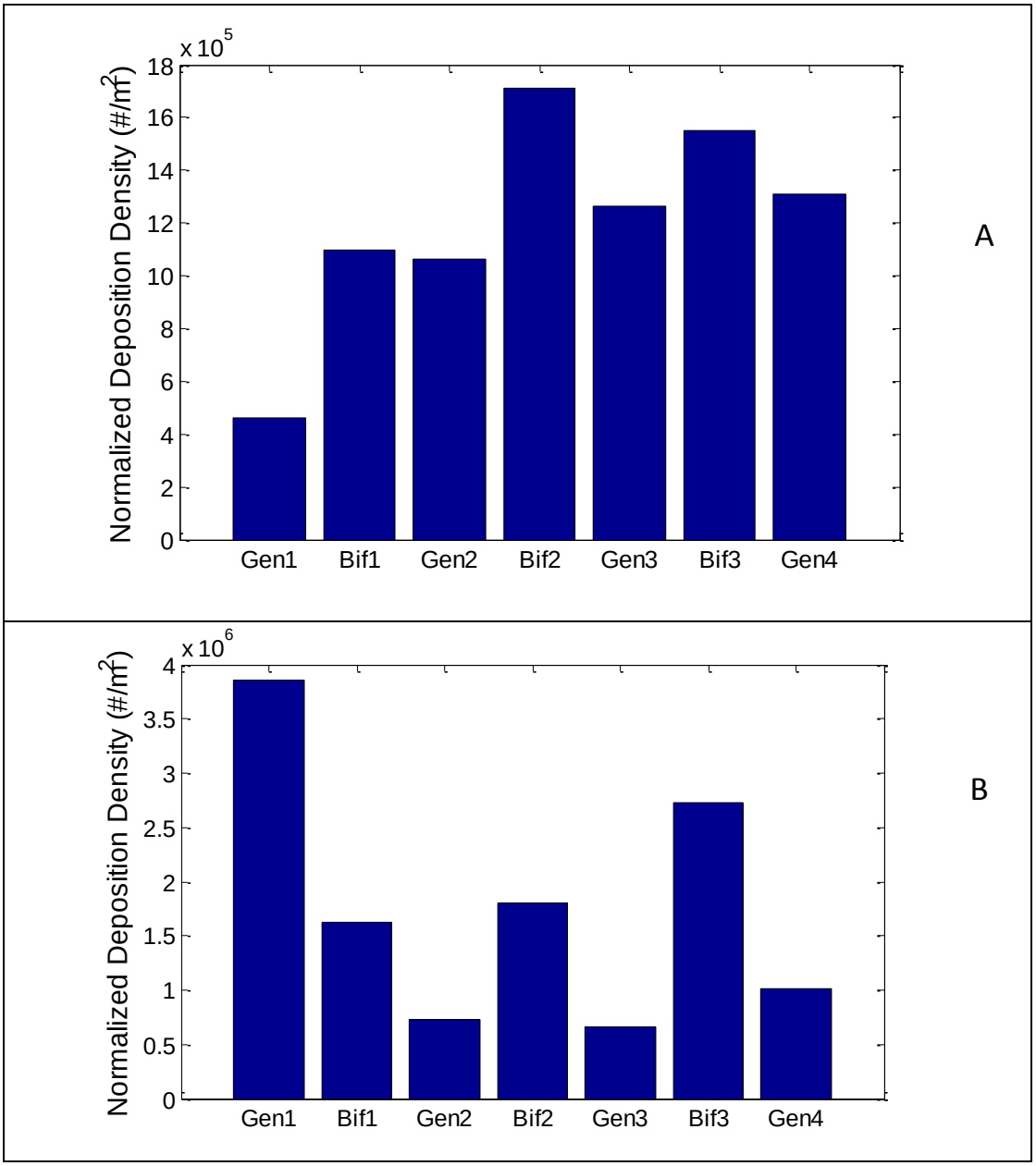

Figure 3.9 Deposition densities of different surface areas (Gen1, Bif1, Gen2, Bif2, Gen3, Bif3 and Gen4) of original geometry under A. steady 0.1 m/s flow; B. pulsatile flow condition.

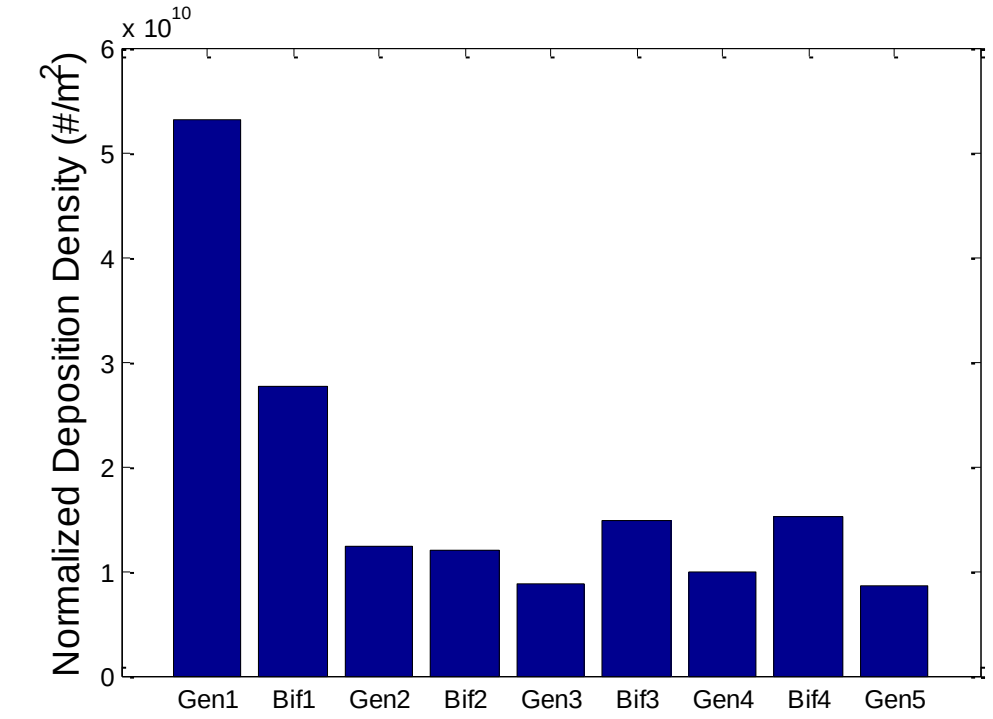

Figure 3.10 Deposition densities of different surface areas of artificial vein model under steady 0.0176m/s flow.

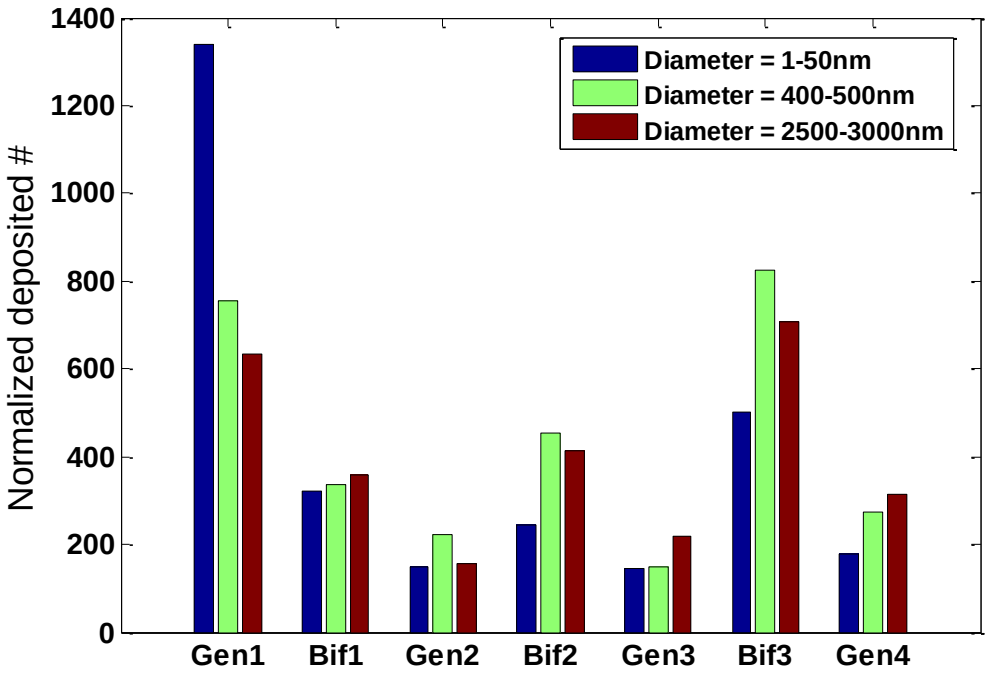

Figure 3.11 Normalized deposited number of particles with different diameter ranges depositing on various regions of original geometry.

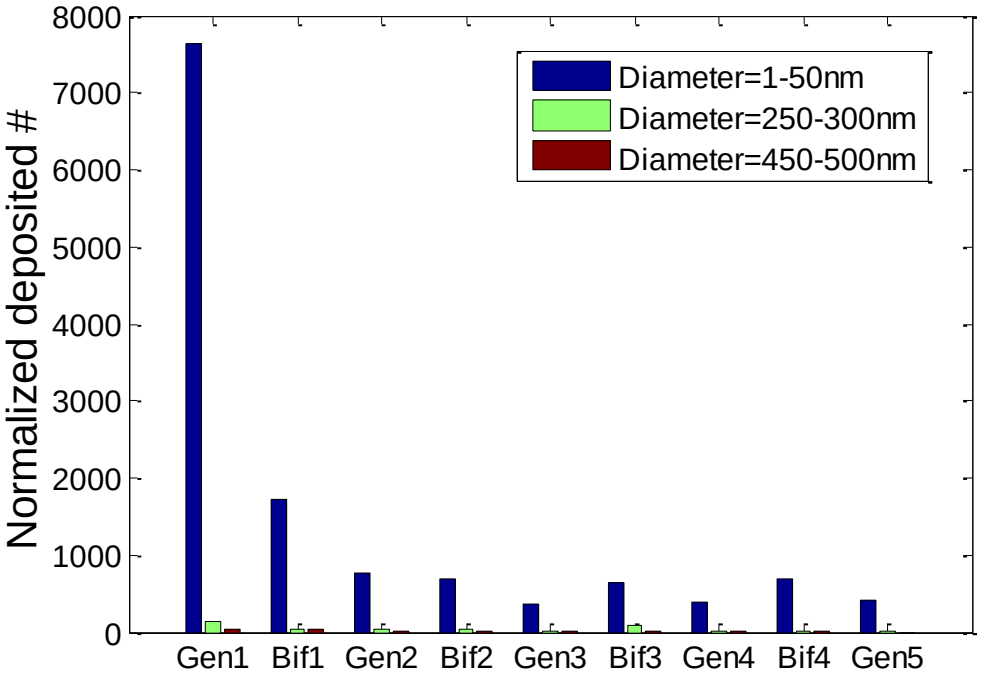

Figure 3.12 Normalized deposited number of particles with different diameter ranges depositing on various regions of artificial vein geometry.

Particle distribution pattern over time is shown in Fig. 3.13. At early stages of particle injection into blood stream, majority of particles are trapped at bifurcation sites first. As time goes, those particles close to vessel wall under low flow speed would also have the chance to diffuse to luminal sections.

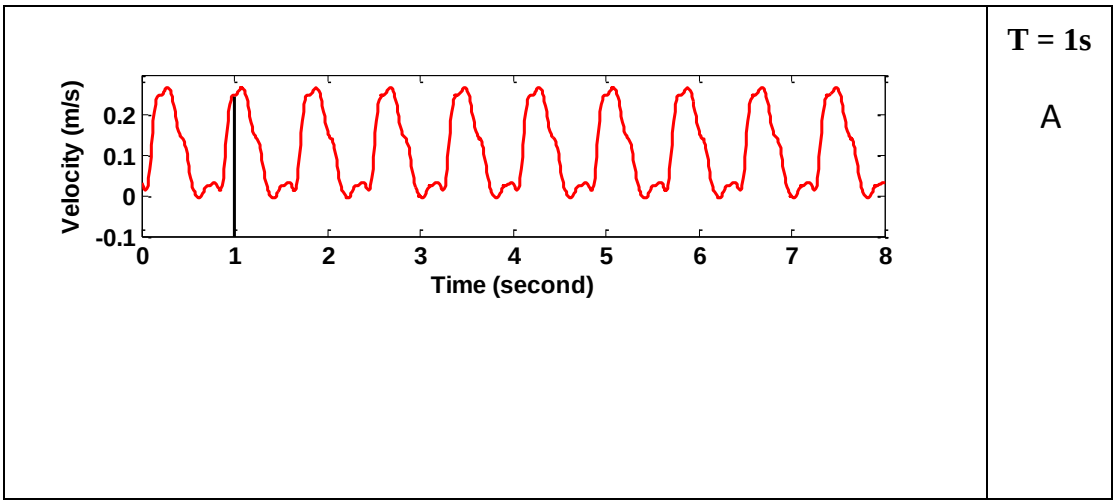

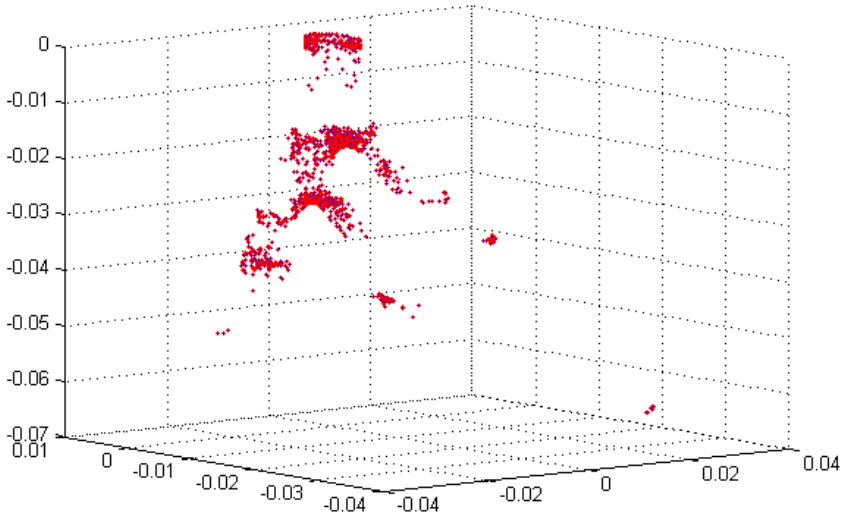
0
-0.01
-0.02
-0.03
-0.04
-0.05
-0.06
-0.07
0.01
0
-0.01
-0.02
-0.03
-0.04
-0.04
-0.02
0
0.02
0.04

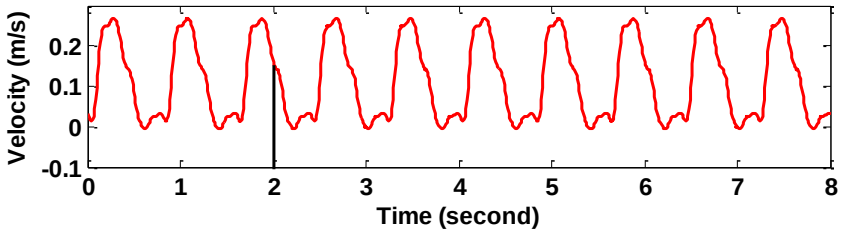
Velocity (m/s)
0.2
0.1
0
-0.1
0
1
2
3
4
5
6
7
8
Time (second)

T = 2s

B

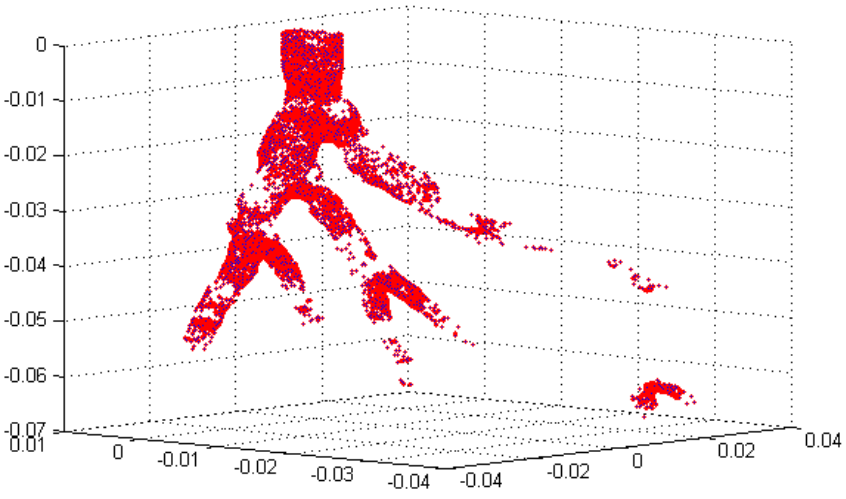
0
-0.01
-0.02
-0.03
-0.04
-0.05
-0.06
-0.07
0.01
0
-0.01
-0.02
-0.03
-0.04
-0.04
-0.02
0
0.02
0.04

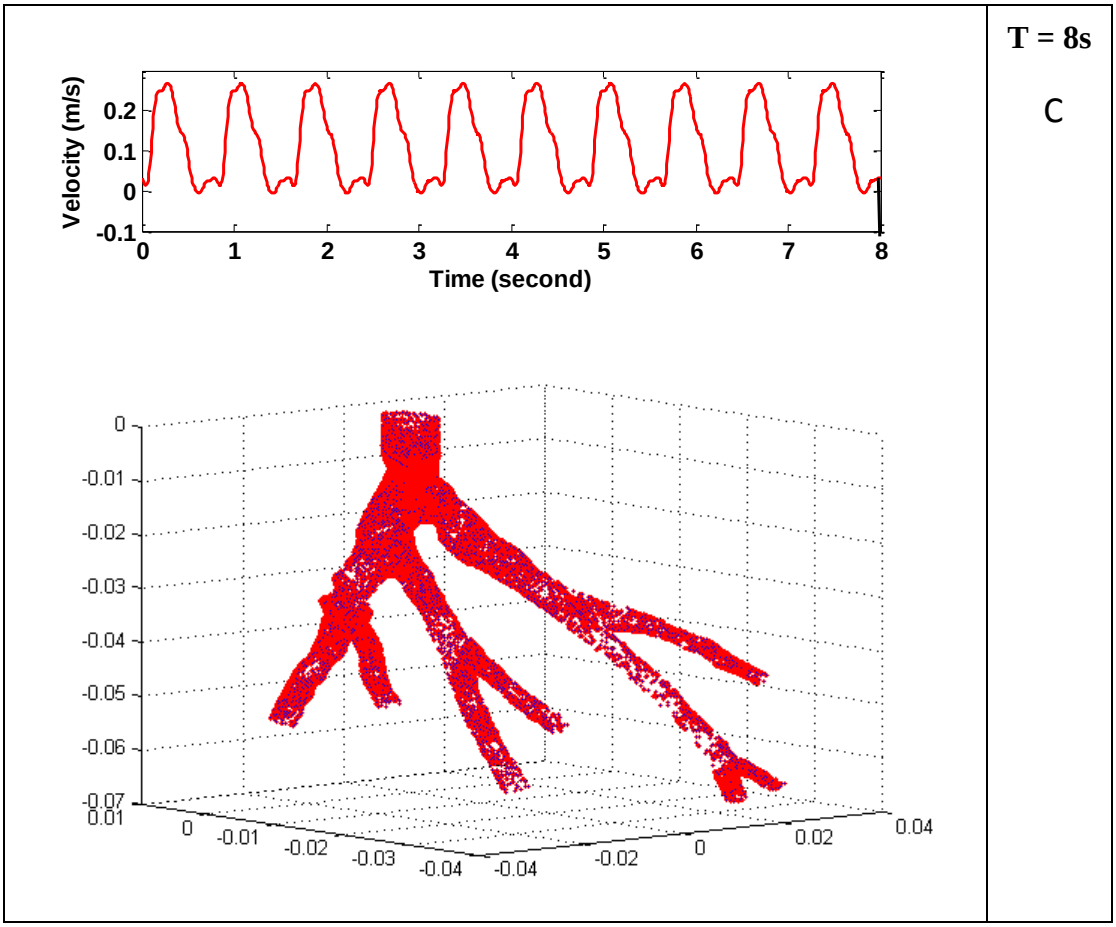

Figure 3.13 3-D representation for trapped location of injected particles in different times A. 1s B. 2s C. 8s after starting the simulation with cardiac inlet flow.

Chapter 4

Conclusion and Future work

4.1 Conclusion

Numerical modeling of targeted drug delivery provides a quantitative description for drug transport and deposition in biological system. Thus, it can be used to evaluate efficiency of drug delivery in medicine treatment. To characterize the particle transport and deposition mechanism, a 4 generations realistic pulmonary vasculature was reconstructed and utilized in the numerical simulation. Proper boundary conditions for flow field and binding mechanism of particles have been defined. It should be noted that the method introduced in this thesis can also be used in larger vascular network reconstruction.

The influence of particle size has been studied quantitatively. The simulation result shows that smaller particles have more chance of binding on vascular wall. The reason of that is the relatively strong Brownian motion and binding probability of smaller particles. But unlike the particle transportation in airflow, the diffusion effect of particle is not so strong. We cannot see the obvious relationship between particle size and distribution pattern in blood flow. The deposition fraction increase with the branch generation order for all sizes particles from generation 2. This is different from particle transportation in airflow, where smaller particles stay more easily at upper region, due to the strong diffusivity.

Vascular geometry, as another key factor, has been studied too. One symmetric artificial geometry and one over-smoothed realistic geometry have been utilized to make comparison with the original geometry. The results show different deposition fractions of different geometries. Particles are more easily to bind at realistic surface. It should be attributed to the fluid flow in the geometry with irregular surface. Due to the

vortices in realistic vascular geometry, the residual time of particles is longer than that in symmetric regular artificial geometry. Also, due to this reason, fluid is mixed well. Thus particles injected in the center have more chance to get closed to the vascular wall. So, to better predict the drug delivery efficiency in medicine treatment, realistic vascular geometry is necessary.

Blood flow pattern also has significant influence on the particle transport and deposition. In this study, both steady flow and pulsatile flow have been studied. In steady flow cases, particle deposition fraction decreases with the increase flow velocity. Particle distribution is nearly uniform on different locations. Whereas, in pulsatile flow cases, particles deposition concentrates at bifurcation areas, where flow velocity is also higher. It should be noticed that the flow pattern also strongly depend on the shape of geometry. No vortex has been found in artificial model, though the inlet flow velocity is also pulsatile.

In summary, the diffusion effect of particle in blood is not as strong as that in airflow. The main loss mechanism is impaction. The particle transport and deposition depend significantly on the particle size, vascular geometry shape and flow pattern. Such knowledge may help to shorten the cycle for design of the smart drug carrier and time to realize the personalized treatment for different patients.

4.2 Future Work

Though the method above is suitable to reconstruct multi-scale vascular geometry, only a 4 generation subunit of whole lung model is chosen to be used in this study. The reason is that large model needs high computation cost. Prior experience shows that an absolute minimum of 10,000-15,000 elements would be required to simulate each tubular portion and an associated bifurcation successfully [35]. Thus, a successful simulation for entire lung would require an equivalent number of elements in each of the 10^7 branches of the lung, which means more than 200GB RAM is necessary. One alternative solution to predict the drug delivery efficiency in relatively complete lung vasculature for particular patient is to cut a sample path of vasculature which we are

interested at, and either combine them with proper boundary conditions or couple with 1-D vascular model.

In addition, to better simulate the motion of nano or micron size particles in blood vessel, blood components, like the red blood cell (RBC) should not be neglected. Without a proper consideration of RBCs, the deposition fraction of drug particles would be lower estimated. It has been reported that RBCs significantly influence the particles dispersion [26]. RBCs and their interaction with fluid flow will be modeled by Immersed Finite Element Method (IFEM) formulation. An advanced model including all these factors will be developed in future.

After all these achieved, model predictions will be validated against experimental and clinic data. Thus, the ultimate goal of this study would be given patient vascular network, to design drug carriers and personalized treatment to maximize the drug delivery efficiency, and minimize the drug dosage and side effects for each individual patient.

References

1. Ghilzai NK. Pulmonary drug delivery-A Review, Midwestern University
2. Mahmud A, Discher DE. 2011. Lung vascular targeting through inhalation delivery: insight from filamentous viruses and other shapes. IUBMB life 63: 607-12
3. Chauvierre C, Labarre D, Couvreur P, Vauthier C. 2003. Novel polysaccharide-decorated poly (isobutyl cyanoacrylate) nanoparticles. Pharmaceutical research 20: 1786-93
4. Mathiowitz E, Jacob JS, Jong YS, Carino GP, Chickering DE, et al. 1997. Biologically erodable microspheres as potential oral drug delivery systems. Nature 386: 410-14
5. Roney C, Kulkarni P, Arora V, Antich P, Bonte F, et al. 2005. Targeted nanoparticles for drug delivery through the blood–brain barrier for Alzheimer's disease. Journal of Controlled Release 108: 193-214
6. Sukhorukov GB, Möhwald H. 2007. Multifunctional cargo systems for biotechnology. TRENDS in Biotechnology 25: 93-98
7. Shah P. 2006. Use of nanotechnologies for drug delivery. MRS bulletin 31: 894-99
8. Nasongkla N, Bey E, Ren J, Ai H, Khemtong C, et al. 2006. Multifunctional polymeric micelles as cancer-targeted, MRI-ultrasensitive drug delivery systems. Nano letters 6: 2427-30
9. Farokhzad OC, Langer R. 2006. Nanomedicine: developing smarter therapeutic and diagnostic modalities. Advanced drug delivery reviews 58: 1456-59
10. Liu Y, Lü W, Zhang Q. 2006. [Recent advances in liposomes and nanoparticles as drug carriers for drug delivery]. Zhongguo yi xue ke xue yuan xue bao. Acta Academiae Medicinae Sinicae 28: 583-89
11. Sharma G, Anabousi S, Ehrhardt C, Ravi Kumar M. 2006. Liposomes as targeted drug delivery systems in the treatment of breast cancer. Journal of drug targeting 14: 301-10
12. Maysinger D, Lovrić J, Eisenberg A, Savić R. 2007. Fate of micelles and quantum dots in cells. European Journal of Pharmaceutics and Biopharmaceutics 65: 270-81
13. Sutton D, Nasongkla N, Blanco E, Gao J. 2007. Functionalized micellar systems for cancer targeted drug delivery. Pharmaceutical research 24: 1029-46
14. Torchilin V. 2004. Targeted polymeric micelles for delivery of poorly soluble drugs. Cellular and Molecular Life Sciences CMLS 61: 2549-59
15. Gao X, Yang L, Petros JA, Marshall FF, Simons JW, Nie S. 2005. < i> In vivo</i> molecular and cellular imaging with quantum dots. Current Opinion in Biotechnology 16: 63-72
16. Smith AM. 2006. Engineering luminescent quantum dots for in vivo molecular and cellular imaging. Ann Biomed Eng 34: 3-14
17. Koenig S, Chechik V. 2006. Shell cross-linked Au nanoparticles. Langmuir 22: 5168-73
18. Lou X, Wang C, He L. 2007. Core-shell Au nanoparticle formation with DNA-polymer hybrid coatings using aqueous ATRP. Biomacromolecules 8: 1385-90
19. Yang Y, Nogami M, Shi J, Ruan M. 2005. Template guided self-assembling two-dimensional array of au@ sio2 core-shell nanoparticles for room-temperature single electron transistors. Journal of nanoscience and nanotechnology 5: 179-83
20. Cheng Y, Gao Y, Rao T, Li Y, Xu T. 2007. Dendrimer-based prodrugs: design, synthesis, screening and biological evaluation. Combinatorial chemistry & high throughput screening 10: 336-49
21. Duncan R, Izzo L. 2005. Dendrimer biocompatibility and toxicity. Advanced drug delivery

reviews 57: 2215-37
22. Najlah M, D'Emanuele A. 2006. Crossing cellular barriers using dendrimer nanotechnologies. Current Opinion in Pharmacology 6: 522-27
23. Editorial. 2006. Nanomedicine: A matter of rhetoric? Nat Materials 5: 243
24. MA Ratner DR. 2002. Nanotechnology: A Gentle Introduction to the Next Big Idea
25. Shah S. 2009. Numerical simulation of particle adhesion dynamics for applications in Nanomedicine and Biosensing.
26. Liu Y, Shah S, Tan J. 2012. Computational modeling of nanoparticle targeted drug delivery. Reviews in Nanoscience and Nanotechnology 1: 66-83
27. Geng Y, Dalhaimer P, Cai S, Tsai R, Tewari M, et al. 2007. Shape effects of filaments versus spherical particles in flow and drug delivery. Nature Nanotechnology 2: 249-55
28. Chen T, Yang M, Wang X, Tan LH, Chen H. 2008. Controlled assembly of eccentrically encapsulated gold nanoparticles. Journal of the American Chemical Society 130: 11858-59
29. Djohari H, Dormidontova EE. 2009. Kinetics of nanoparticle targeting by dissipative particle dynamics simulations. Biomacromolecules 10: 3089-97
30. Gref R, Minamitake Y, Peracchia MT, Trubetskoy V, Torchilin V, Langer R. 1994. Biodegradable long-circulating polymeric nanospheres. Science 263: 1600-03
31. Tan J, Wang S, Yang J, Liu Y. 2013. Coupled particulate and continuum model for nanoparticle targeted delivery. Computers & structures 122: 128-34
32. Asgharian B, Hofmann W, Bergmann R. 2001. Particle deposition in a multiple-path model of the human lung. Aerosol Science & Technology 34: 332-39
33. Lai T, Morsi Y, Mazumdar J. 2002. Modelling and Simulation of Particle Deposition in the Human Lung. Profiles in Industrial Research Knowledge and Innovation: 313-20
34. Johnston BM, Johnston PR, Corney S, Kilpatrick D. 2006. Non-Newtonian blood flow in human right coronary arteries: transient simulations. Journal of biomechanics 39: 1116-28
35. Nowak N, Kakade PP, Annapragada AV. 2003. Computational fluid dynamics simulation of airflow and aerosol deposition in human lungs. Annals of biomedical engineering 31: 374-90
36. Pellot C, Herment A, Sigelle M, Horain P, Maitre H, Peronneau P. 1994. A 3D reconstruction of vascular structures from two X-ray angiograms using an adapted simulated annealing algorithm. Medical Imaging, IEEE Transactions on 13: 48-60
37. Flórez-Valencia L, Orkisz M, Montagnat J. 2004. 3D graphical models for vascular-stent pose simulation. Machine Graphics and vision 13: 235-48
38. Schroeter JD, Kimbell JS, Asgharian B, Tewksbury EW, Singal M. 2012. Computational fluid dynamics simulations of submicrometer and micrometer particle deposition in the nasal passages of a Sprague-Dawley rat. Journal of aerosol science 43: 31-44
39. Chern M-J, Wu M-T, Her S-W. 2012. Numerical study for blood flow in pulmonary arteries after repair of tetralogy of Fallot. Computational and mathematical methods in medicine 2012
40. Zhang Z, Kleinstreuer C, Donohuec JF, Kim CS. 2005. Comparison of micro- and nano-size particle depositions in a human upper airway model. Journal of Aerosol Science 36: 211-33
41. Decuzzi P, Ferrari M. 2006. The adhesive strength of non-spherical particles mediated by specific interactions. Biomaterials 27: 5307-14
42. Delaunay B. 1934. Sur la sphere vide. Izv. Akad. Nauk SSSR, Otdelenie Matematicheskii i Estestvennyka Nauk 7: 1-2
43. Olufsen MS, Nadim A. 2004. On deriving lumped models for blood flow and pressure in the

systemic arteries. Math Biosci Eng 1: 61-80
44. Ermak DL, McCammon J. 2008. Brownian dynamics with hydrodynamic interactions. The Journal of chemical physics 69: 1352-60
45. Einstein A. 1956. Investigations on the Theory of the Brownian Movement: Courier Dover Publications
46. Savithiri S, Pattamatta A, Das SK. 2011. Scaling analysis for the investigation of slip mechanisms in nanofluids. Nanoscale research letters 6: 1-15
47. Goldman A, Cox R, Brenner H. 1967. Slow viscous motion of a sphere parallel to a plane wall—II Couette flow. Chemical Engineering Science 22: 653-60
48. Henk CB, Schlechta B, Grampp S, Gomischek G, Klepetko W, Mostbeck GH. 1998. Pulmonary and aortic blood flow measurements in normal subjects and patients after single lung transplantation at 0.5 T using velocity encoded cine MRI. CHEST Journal 114: 771-79
49. Strahler AN. 1952. Hypsometric (area-altitude) analysis of erosional topography. Geological Society of America Bulletin 63: 1117-42
50. Kassab GS, Rider CA, Tang NJ, Fung Y-CB. 1993. Morphometry of pig coronary arterial trees. American Journal of Physiology 265: H350-H50
51. Huang W, Yen R, McLaurine M, Bledsoe G. 1996. Morphometry of the human pulmonary vasculature. Journal of Applied Physiology 81: 2123-33
52. Spilker RL, Feinstein JA, Parker DW, Reddy VM, Taylor CA. 2007. Morphometry-based impedance boundary conditions for patient-specific modeling of blood flow in pulmonary arteries. Annals of biomedical engineering 35: 546-59

Vita

The author was born in China in 1988. He was awarded bachelor degree with honor in Mechanical Engineering in Dalian University of Technology in 2011. Following that, he spent two years in studying Mechanical Engineering in Lehigh University. During that, he joined Bio-Nanomechanics lab to investigate nanoparticle transport and binding behavior using both computational and experimental approaches. By 2014, he finished his M.S. project in Lehigh University.